

Diagnosing Pathologic Myopia by Identifying Posterior Staphyloma and Myopic Maculopathy Using Ultra-Widefield Images with Deep Learning

Peiwu Qin

pwqin@sz.tsinghua.edu.cn

Tsinghua University

Yang Liu

Tsinghua University

Keming Zhao

Shenzhen Eye Hospital, Jinan University, Shenzhen Eye Institute

Lihui Luo

Institute of Biopharmaceutics and Health Engineering, Tsinghua Shenzhen International Graduate School

Ziheng Zhang

Institute of Biopharmaceutics and Health Engineering, Tsinghua Shenzhen International Graduate School

Zhenghang Qian

Department of Automation, Tsinghua University

Cenk Jiang

Institute of Biopharmaceutics and Health Engineering, Tsinghua Shenzhen International Graduate School

Zhicheng Du

Institute of Biopharmaceutics and Health Engineering, Tsinghua Shenzhen International Graduate School

Simin Deng

Shenzhen Eye Hospital, Jinan University, Shenzhen Eye Institute

Chengming Yang

Southern University of Science and Technology Hospital

Duanpo Wu

Hangzhou Dianzi University

Shuai Wang

Hangzhou Dianzi University

Xingru Huang

Hangzhou Dianzi University

Chenggang Yan

Hangzhou Dianzi University

Yingting Zhu

State Key Laboratory of Ophthalmology, Zhongshan Ophthalmic Center, Sun Yat-sen University,
Guangdong Provincial Key Laboratory of Ophthalmology Visual Science, Guangdong Provincial Clinical
Research

Yehong Zhuo

State Key Laboratory of Ophthalmology, Zhongshan Ophthalmic Center, Sun Yat-sen University,
Guangdong Provincial Key Laboratory of Ophthalmology Visual Science, Guangdong Provincial Clinical
Research

Chunsheng Qu

Clinical Laboratory of Lishui People's Hospital, First Affiliated Hospital of Lishui College, Wenzhou
Medical College Lishui Hospital

Jiaqi Chen

Clinical Laboratory of Lishui People's Hospital, First Affiliated Hospital of Lishui College, Wenzhou
Medical College Lishui Hospital

Zhenqiang Huang

Clinical Laboratory of Lishui People's Hospital, First Affiliated Hospital of Lishui College, Wenzhou
Medical College Lishui Hospital

Chenying Lu

Zhejiang Key Laboratory of Imaging and Interventional Medicine, Department of Radiology, Lishui
Central Hospital, The Fifth Affiliated Hospital of Wenzhou Medical University

Minjiang Chen

Zhejiang Key Laboratory of Imaging and Interventional Medicine, Department of Radiology, Lishui
Central Hospital, The Fifth Affiliated Hospital of Wenzhou Medical University

Dongmei Yu

School of Mechanical, Electrical \& Information Engineering, Shandong University

Jiantao Wang

Shenzhen Eye Hospital, Jinan University, Shenzhen Eye Institute

Jiansong Ji

Zhejiang Key Laboratory of Imaging and Interventional Medicine, Department of Radiology, Lishui
Central Hospital, The Fifth Affiliated Hospital of Wenzhou Medical University

Article

Keywords:

Posted Date: November 29th, 2024

DOI: <https://doi.org/10.21203/rs.3.rs-5421907/v1>

License:  This work is licensed under a Creative Commons Attribution 4.0 International License.

[Read Full License](#)

Additional Declarations: No competing interests reported.

¹ Diagnosing Pathologic Myopia by Identifying
² Posterior Staphyloma and Myopic Maculopathy
³ Using Ultra-Widefield Images with Deep Learning

⁴ Yang Liu^{1,7†}, Keming Zhao^{1,2†}, Lihui Luo¹, Ziheng Zhang¹,
⁵ Zhenghang Qian^{1,4}, Cenk Jiang¹, Zhicheng Du¹, Simin Deng²,
⁶ Chengming Yang⁵, Duanpo Wu⁶, Shuai Wang⁶, Xingru Huang⁶,
⁷ Chenggang Yan⁶, Yingting Zhu⁸, Yehong Zhuo⁸, Chunsheng Qu⁹,
⁸ Jiaqi Chen⁹, Zhenqiang Huang⁹, Chenying Lu¹⁰, Minjiang Chen¹⁰,
⁹ Dongmei Yu⁷, Jiantao Wang^{2*}, Peiwu Qin^{1,3*}, Jiansong Ji^{10*}

¹⁰ ¹Institute of Biopharmaceutics and Health Engineering, Tsinghua Shenzhen
¹¹ International Graduate School, Shenzhen, 518055, China.

¹² ²Shenzhen Eye Hospital, Jinan University, Shenzhen Eye Institute, Shenzhen, 518055,
¹³ China.

¹⁴ ³Center of Precision Medicine and Healthcare, Tsinghua-Berkeley Shenzhen Institute,
¹⁵ Shenzhen, 518055, China.

¹⁶ ⁴Department of Automation, Tsinghua University, Beijing, 100084, China.

¹⁷ ⁵Southern University of Science and Technology Hospital, Shenzhen, 518055, China.

¹⁸ ⁶Hangzhou Dianzi University, Hangzhou, Zhejiang, 310018, China.

¹⁹ ⁷School of Mechanical, Electrical & Information Engineering, Shandong University,
²⁰ Weihai, 264209, China.

²¹ ⁸State Key Laboratory of Ophthalmology, Zhongshan Ophthalmic Center, Sun
²² Yat-sen University, Guangdong Provincial Key Laboratory of Ophthalmology Visual
²³ Science, Guangdong Provincial Clinical Research Center for Ocular Diseases,
Guangzhou, 510060, China.

²⁴ ⁹Clinical Laboratory of Lishui People's Hospital, First Affiliated Hospital of Lishui
College, Wenzhou Medical College Lishui Hospital, Lishui, Zhejiang, 323000, China.

²⁵ ¹⁰Zhejiang Key Laboratory of Imaging and Interventional Medicine, Department of
Radiology, Lishui Central Hospital, The Fifth Affiliated Hospital of Wenzhou Medical
University, Lishui, Zhejiang, 323000, China.

³⁰ *Corresponding author(s). E-mail(s): wangjiantao65@126.com;

³¹ pwqin@sz.tsinghua.edu.cn; jjstcty@wmu.edu.cn;

³² Contributing authors: lyang22@mails.tsinghua.edu.cn;

³³ 542807062@qq.com;

³⁴ [†]These authors contributed equally to this work.

Abstract

Pathologic myopia (PM) has long been a leading cause of visual impairment and blindness. While numerous deep learning-based approaches have improved the efficiency and accuracy of recognizing PM, few have thoroughly investigated clinically significant pathological patterns due to the scarcity of datasets with lesion-wise labeling, particularly those comprising ultra-widefield (UWF) images that encompass a broader retinal field of view. In this study, we gather a large-scale multi-source ultra-widefield imaging myopia dataset, PSMM, labeled with posterior staphyloma (PS) and myopic maculopathy (MM). Compared with traditional colored fundus photography, UWF images exhibit informative characteristics concerning peripheral lesions caused by axial elongation and structural deformation in eyes with pathologic myopia. The labels obtained from the dataset can substantially assist in the progression diagnosis of pathologic myopia and guide prognosis. We introduce an end-to-end lightweight framework called RealMNet, which precisely identifies these challenging pathological patterns underpinned by a well-curated dataset. RealMNet is more adaptable to medical devices with only 21 million parameters compared to existing approaches. Through extensive experiments on a unified platform using all-around metrics regarding bipartitions and rankings across three experimental protocols, we demonstrate the robustness and generalizability of RealMNet, showcasing promising merit in clinical applications.

56 1 Introduction

The increasing prevalence of myopia worldwide is a significant public health concern [1]. It is projected that by 2050, nearly 50% of the global population will be affected. Myopia, defined by a spherical equivalent (SE) ≤ -0.5 diopters, can lead to visual impairments that greatly reduce patients' quality of life and impose substantial economic burdens [2]. All degrees of myopia pose potential risks for adverse changes in ocular tissues, especially at high levels of myopia (defined as spherical equivalent worse than -5.0 or -6.0 diopters) and pathologic myopia (resulting in irreversible visual impairment or blindness due to pathological retinal changes secondary to high myopia) [3]. Ophthalmic examinations, typically involving fundus imaging, are necessary for detecting and diagnosing relevant fundus lesions. While traditional color fundus photography (CFP) captures the retina within 30–60 degrees, novel imaging modalities such as ultra-widefield (UWF) imaging with a field of view ranging from 100 to 200 degrees [4], can capture retinal lesions missed by CFP, leading to improved screening accuracy and early detection. Despite the increasing use of advanced retinal imaging in ophthalmic practices, publicly available UWF datasets remain scarce, which hinders the development of diagnostic and support systems needed to help clinicians interpret these advanced imaging modalities.

Recent advancements in deep learning (DL) have made it possible to automatically process medical images for various tasks, achieving performance comparable to human experts. In the case of retinal diseases, DL models not only accurately diagnose

and monitor conditions such as diabetic retinopathy and age-related macular degeneration from retinal images [5–7], but also assist in developing personalized treatment plans. In addition, DL has been applied to myopia-related screening, assessing the risk of myopia progression by analyzing retinal images and enabling early intervention. Although these methods are robust, there is a need for more investigation into sophisticated pathological patterns. A system called the Meta-Analysis of Pathologic Myopia (META-PM) [8] categorizes myopic atrophic components into five classes: no myopic retinal lesions (Grade 0), tessellated fundus only (Grade 1), diffuse chorioretinal atrophy (Grade 2), patchy chorioretinal atrophy (Grade 3), and macular atrophy (Grade 4). Pathologic myopia is now defined as myopic maculopathy (according to META-PM criteria: grade 2 or above) or posterior staphyloma [9]. Posterior staphyloma manifests as an outpouching of the ocular wall, with a curvature radius less than that of the surrounding sclera. PS often leads to changes in the retina, choroid, and nerve fiber layer, subsequently affecting the patient's vision. Early identification of PS is crucial because it can lead to severe complications, such as retinal detachment, macular hemorrhage, and choroidal neovascularization, all of which may cause irreversible vision loss. MM is one of the primary causes of vision deterioration in patients with high myopia because the macula is the area of the retina with the highest visual acuity, and any damage there can significantly impact vision quality. Early diagnosis and management of these conditions can help slow or prevent disease progression and reduce the risk of vision loss. Existing research has some limitations despite advancements. Firstly, more attention should be given to myopic maculopathy and posterior staphyloma. This is due to the difficulty in identifying their complete contour on CFP accurately, hence identifying these lesions requires high-quality ultra-widefield (UWF) imaging data. UWF imaging allows for precise diagnosis of peripheral lesions and the edges of staphyloma, appearing as a dark gray band-shaped ring with twisted retinal and choroidal vessels. However, the high equipment cost, complex operations, and data acquisition expenses make large-scale UWF data collection challenging for many studies. Secondly, previous studies often use balanced data, ignoring the significant data imbalance in real-world scenarios [10]. Retinal lesions in pathologic myopia are highly heterogeneous and often coexist with other types of retinal lesions, creating imbalanced data and making it more challenging to distinguish PS from MM accurately. Thirdly, detecting PS and MM involves complex multi-label learning tasks, which pose higher demands on algorithm models. Many existing studies focus on identifying a single lesion or simpler pathologies and cannot handle multiple complex coexisting lesions. Thus, traditional imaging data and diagnostic tools may not provide precise classifications, limiting the exploration of these specific lesions. Lastly, there has been a strong focus on building large and complex models [11]. While these models are powerful, due to their size and complexity, they need to be more adaptable for use in medical devices, especially in resource-constrained clinical environments. Therefore, the creation of the PSMM dataset fills these gaps, providing a high-quality data source that supports the precise identification of multiple lesions and clinical research, thereby improving patient diagnosis and treatment outcomes.

Previous studies employing DL models for myopia detection often rely on CFP, assessing only a narrow range of the posterior pole of the retina [12]. However, with

the elongation of the eyeball in highly myopic eyes, the likelihood of peripheral retinal lesions increases significantly, necessitating the use of UWF imaging for comprehensive evaluation [13]. With this in mind, we suggest adopting a recognition system for peripheral retinal lesions: no peripheral lesion (NoPL), lattice degeneration or cystic retinal tuft (LDoCRT), holes or tears (HoT), rhegmatogenous retinal detachment (RRD), and postoperative cases (PC). When combined with UWF imaging, this system allows for a thorough assessment of retinal health in myopic patients. For instance, peripheral lattice degeneration, seen as a white lattice pattern on UWF images due to retinal microvascular occlusion, may develop into various-sized circular atrophic holes over time. These changes are closely associated with rhegmatogenous retinal detachment, potentially giving rise to severe visual impairment [14]. Evaluating peripheral retinal lesions significantly enhances our ability to comprehensively monitor and treat myopic retinal changes by enabling the earlier detection and management of such sight-threatening complications.

In this work, we present a detailed and efficient workflow (Fig. 1) for identifying challenging lesions. We compile a dataset containing UWF images of pathologic myopia with clinically significant lesions from multiple medical sources. Experienced physicians label images related to posterior staphyloma, myopic maculopathy, and peripheral lesions under the guidance of META-PM and double-check annotations to ensure accuracy. With the support of this curated dataset, we are able to identify clinically significant pathological patterns by developing an end-to-end framework called RealMNet that embraces **Real-world Myopia** diagnosis. Thanks to the adoption of a compact and efficient vision transformer [15] as our backbone, the framework is lightweight enough to be applied to modern medical devices. We approach this challenge as a multi-label learning task for two reasons: first, posterior staphyloma may be present with myopic maculopathy, jointly indicating pathologic myopia, and second, peripheral lesions could coexist. We comprehensively evaluate RealMNet’s performance using three distinct experimental protocols: centralized inference, main-source robustness, and cyclic-source generalizability. Under the centralized inference protocol, we compare the inference performance of RealMNet on the PSMM dataset against four pretrained comparison models: DeiT [16], EfficientNet [17], ConvNeXt [18], and Swin Transformer [19]. The other two protocols are used to assess the robustness and generalizability of the model for lesion identification, which is crucial for clinical use. We evaluate labeling efficiency using RealMNet with increasing resolutions and interpret parameters at different stages of the backbone. We demonstrate the effectiveness of regularization techniques used in the proposed method with extensive evaluation experiments. Furthermore, we investigate the potential negative impact of the physical device boundaries present in images captured by modern ultra-widefield imaging, which may impede peripheral information. The boundaries have been segmented out to make sure that the learning process of the model is not compromised. To visually interpret the model’s decision-making for inference, we utilize an improved version of gradient-weighted class activation mapping called Grad-CAM++ that better localizes objects and explains occurrences of multiple objects of a class in a single image [20]. The model performance is reported with all-around measures (details are listed in

166 Evaluation metrics/Supplemental materials) for evaluating both bipartitions and rank-
167 ings concerning the ground truth of multi-label data. All P values are calculated with
168 a two-sided t -test between RealMNet and the other comparison model to check for
169 significance.

170 2 Results

171 2.1 Multi-source curated UWF myopia dataset provides a 172 solid foundation for multi-lesion identification

173 We gathered a specialized dataset called PSMM derived from five distinct hospital
174 sources for identifying posterior staphyloma (PS) and myopic maculopathy (MM) that
175 could assist clinicians in diagnosing pathologic myopia. The PSMM dataset comprised
176 43,371 ultra-widefield images of 4,560 patients who sustained high myopia or patho-
177 logic myopia after data filtering for quality assurance. We also separately managed the
178 five sub-sources that integrated the PSMM dataset to facilitate characteristic research.
179 Generally, the PSMM dataset provided a competitive scale considering the expense of
180 ultra-widefield imaging that captured a broader retinal field of view compared to color
181 fundus photography (Fig. A1a). Experienced clinicians labeled posterior staphyloma
182 with binary annotations to indicate its presence (NoPS or PS) and myopic macu-
183 lopathy with five categories: no myopic retinal lesions (NoMRL), tessellated fundus
184 only (TFO), diffuse chorioretinal atrophy (DCA), patchy chorioretinal atrophy (PCA),
185 and macular atrophy (MA). An intuitive illustration of these pathological patterns
186 can be found in (Fig. A1b). Notably, posterior staphyloma and myopic maculopathy
187 may appear simultaneously, forming multi-label datasets (MLDs). The PSMM dataset
188 exhibits an imbalanced distribution (Fig. 2), as exposed in other retinal diseases, pos-
189 ing a significant challenge to method development. Overall, the PSMM dataset is
190 well-curated on fine-grained multi-lesion recognition and the diagnosis of pathologic
191 myopia, which also provides convenience for those developing deep learning models
192 for recognizing retinal diseases, as well as empowering large-parametric deep learning
193 techniques like foundation models to discern retinal diseases requiring ultra-widefield
194 images.

195 2.2 End-to-end lightweight hybrid framework with 196 optimization mitigates multi-label imbalance issue

197 The imbalance present in multi-label datasets (MLDs) significantly impacts the
198 model's performance, leading to biased learning and inadequate knowledge acquisi-
199 tion. This study presented three techniques to tackle the imbalance issue: resampling
200 methods, classifier adaptation, and cost-sensitive calibration. Cost-sensitive calibra-
201 tion addressed the multi-label imbalance by developing the loss function from Binary
202 Cross-Entropy (BCE) Loss [21], considering that multi-label learning involves decom-
203 posing the multi-label task into multiple binary tasks, each focusing on distinguishing
204 samples within a target class category. We gradually introduced tunable parameters
205 for BCE Loss to alleviate the imbalance issue on the PSMM dataset. Initially, We
206 attempted to train the model using Binary Cross-Entropy (BCE) Loss, and to address

207 class imbalance, we implemented a commonly used weighting factor $\alpha \in [0, 1]$ to form
 208 an α -balanced BCE Loss. In our experiments, we discovered that the model performed
 209 better when using an α value of 0.75 (Table A5), which aligned with its original use
 210 in the dense detection task. We introduced a focusing parameter, γ , to adjust the
 211 loss function and concentrate training on difficult negative samples by reducing the
 212 impact of easy samples [22]. We tested different α values for each candidate focusing
 213 parameter within the list of [0, 0.1, 0.2, 0.5, 1, 2, 5], as recommended in the original lit-
 214 erature. We found that increasing the focusing parameter did not yield any benefits
 215 (Table A6), possibly due to the elimination of gradients from rare positive samples
 216 while devaluing the contribution from easy negatives. To address this issue, we utilized
 217 γ_+ and γ_- to separate the focusing levels of positive and negative samples, allowing
 218 the model to emphasize the positive samples while minimizing the influence of easy
 219 negative samples [23]. The experimentally determined cost-sensitive calibration helps
 220 the model learn from balanced samples (Fig. A4a), ultimately leading to optimal per-
 221 formance with $\gamma_+ = 3$ and $\gamma_- = 4$. We introduced a probability-shifting mechanism to
 222 assess the influence of very easy and mislabeled negative samples. The results showed
 223 that adjusting the shifted probability did not improve the model's performance, indi-
 224 cating that our dataset was well-curated and had minimal errors. We also studied a
 225 state-of-the-art approach called Two-way Loss [24], which is exclusively designed for
 226 multi-label learning. This method uses relative comparison with the softmax function.
 227 We adjusted the margins between positive and negative logits using positive temper-
 228 ature T_P and negative temperature T_N . We evaluated different values for T_P and T_N
 229 within the list of [0.5, 1, 2, 4]. The results (Table A7) showed a similar trend to the
 230 original study, but the best-performing choice still did not outperform our implemen-
 231 tation using asymmetric focusing. Classifier adaptation involves residual attention,
 232 combining class-specific and class-agnostic features during the inference stage [25]. We
 233 introduced a tunable parameter λ to leverage these two types of features, searching
 234 within the range of [0.2, 1.4] with a step of 0.2, as done in the original literature using
 235 Vision Transformer (ViT) as the backbone on the MS-COCO dataset. The residual
 236 attention was extended in a multi-head (H) manner, initially set at $H = 8$. The model
 237 with $\lambda = 1.2$ and $H = 2$ achieved better mean Average Precision (mAP) compared to
 238 other settings while maintaining similar performance on other evaluation metrics A4.

239 **2.3 Multi-protocol experiments demonstrate valued inference** 240 **with robustness and generalizability**

241 We devised three distinct experimental protocols 1c to excavate the model's inference
 242 capacity, robustness, and generalizability (see detailed strategies in 'Experimental pro-
 243 tocols'). The results (Fig. 3a) under the centralized inference protocol revealed that
 244 RealMNet outperformed ($P < 0.001$) all other benchmark approaches on F1 Score
 245 with 0.7903 (95% CI 0.7531-0.8275), mAP with 0.8398 (95% CI 0.7923-0.8873), and
 246 AUROC with 0.9736 (95% CI 0.9682-0.9791). Unless otherwise noted, these three met-
 247 rics were considered the primary criteria for measuring the model's performance. We
 248 additionally presented other evaluation metrics for complementary analysis ('Evalua-
 249 tion metrics' in Methods). RealMNet achieved the lowest Coverage of 2.2586 (95% CI
 250 2.2204-2.2968), significantly surpassing ($P < 0.001$) other models, indicating that the

proposed model could better approximate the realistic situation. Precision and Recall were two opposite measures, with one tending to be high and the other low. In our case, we preferred a superior Recall for developing a discrimination model that would identify as many potential positive samples as possible to aid in screening. Guided by the main-source robustness protocol, we discovered that the model trained exclusively on the main subset could reliably identify posterior staphyloma and myopic maculopathy on auxiliary subsets in general (Fig. 3b). On the other hand, it illustrated abundant task-specific knowledge implied in the primary source data. RealMNet represented robustness on the SUSTech subset, achieving an F1 Score of 0.7956 (95% CI 0.7187-0.8724), mAP of 0.8927 (95% CI 0.8211-0.9642), and AUROC of 0.9869 (95% CI 0.9830-0.9908). Even when tested on the Zhongshan subset whose hard negative samples may impeded model inference, our model still maintained acceptable performance (mean value) with an F1 score of over 70%, mAP over 80%, and AUROC over 95%. When examined under the cyclic-source generalizability protocol, RealMNet exhibited similar performance to that under the main-source robustness protocol (Fig. 3c), reflecting its stable exertion when additional information was introduced. On the Zhongshan subset, the model displayed difficulty in correctly distinguishing a small fraction of label pairs, as evidenced by a Hamming Loss of 0.0985 (95% CI 0.0898-0.1072) and a Ranking Loss of 0.0530 (95% 0.0467-0.0593). This could be attributed to a relatively high Coverage value, indicating that the model required more steps to infer all relevant labels for the samples (posterior staphyloma and myopic maculopathy).

2.4 Interpretable workflow facilitates convincing diagnosis of pathologic myopia in clinical application

Even though deep learning methods offer powerful capacities, they are commonly known as black boxes due to their intricate inference mechanisms [26]. To be useful in clinical applications, these methods need to be not only efficient but explainable and trustworthy. Labeling efficiency refers to the amount of training data and labels required to achieve a certain level of performance for a given task, which shows the annotation workload for medical experts [11]. RealMNet achieves precise identification even with only half of the training resources (Fig. 4a), demonstrating its capability to capture clinically significant pathological patterns at a low-level feature space. RealMNet-384 exemplified a remarkable improvement (mean value) in F1 Score by 10%, mAP by 10%, and AUROC by 1%, despite an increase in labeling from 20% to 50%. Although the RealMNet-224 and the RealMNet-384 performed similarly as more training data was used, RealMNet-512 consistently achieved superior performance, demonstrating the non-trivial benefits of abundant information involved in higher resolution. The model could have gained even slightly higher performance when using ninety percent of the training resources; we insisted that the model trained on all available data eliminate the variability and produce unbiased results. We aimed to assess the contribution of each stage of the used backbone by measuring parameter efficiency (Fig. 4b). Freezing the first one or two layers of the model did not decrease performance, indicating that the model retained low-level general features from pretraining distillation on large-scale natural image datasets (e.g., ImageNet-21k). However, the performance of RealMNet dropped significantly when the first three or four layers

were frozen, indicating that the model still required high-level features related to pathological patterns. Furthermore, we observed the efficacy of the regularization used in this study. Augmentation is a crucial regularization technique widely adopted in deep learning-based approaches to augment training data to avoid overfitting, especially when the amount of training data is not large enough in many tasks of medical fields. We explored the impact of the proposed simulated augmentation and batch-wise augmentation (Fig. 4c) and found that employing these two types of augmentation techniques brought a gain of 3.5% on F1 Score, 6.7% on mAP, and 3.2% on AUROC, respectively (w/o Aug vs. Aug). The simulated augmentation was used to mirror real-world situations. The model’s performance decreased significantly when the simulated augmentation was removed (w/o SA vs. Aug). This suggested that the model was trained with overly optimistic and simplistic objectives because the training data did not represent real-world scenarios. Batch-wise augmentation involved enhancing synthetic samples by interweaving two samples. Removing batch-wise augmentation did not cause a significant loss (w/o BA vs. Aug), indicating that the model had inherently been adequate to build intra- and inter-affinities between pathological patterns. A slight decrease in Ranking Loss and Coverage suggested that batch-wise augmentation helped the model learn more accurate label distributions. Drop path [27] is another regularization technique that markedly circumvents the overfitting issue by randomly dropping the neural path of the network. We used the drop path because of the overfitting hazard caused by a relatively small scale of training data (Fig. A5c). To interpret the panoramic focusing capacity of RealMNet, we considered the potential negative impact of the physical device boundaries inevitably imaged along with the imaging targets by modern ultra-widefield imaging, which may occlude partial information. The comparative experimental results (Fig. A6b) showed that RealMNet was not affected by these barriers, demonstrating its outstanding focusing ability. Visual interpretability has been widely recognized as an intuitive representation of the decision-making process in deep learning techniques. We adopted an improved version of gradient-weighted class activation mapping (Grad-CAM++) [20] that localized objects better and explained occurrences of multiple objects of a class in a single image. We generated visualizations of random samples for each category using RealMNet (Fig. 5). These heatmaps revealed irregular attentive regions corresponding to diffused pathological patterns embodied in different lesion levels, manifesting the explainable learning of the proposed model.

3 Discussion

In this study, we introduced a novel perspective for assisting in diagnosing pathological myopia by means of identifying posterior staphyloma and myopic maculopathy using ultra-widefield images with deep learning. We found that there have been many studies dedicated to the application of deep learning to assist myopia diagnosis [28, 29]. However, the majority of these studies overlooked exclusive discrimination mechanisms due to a lack of specialized datasets built on ophthalmological expertise. Pathologic myopia has been broadly recognized as myopic maculopathy with meticulously defined

337 categories or with the presence of posterior staphyloma [30]. Nonetheless, to our knowl-
338 edge, limited research has thoroughly examined these lesions, and there are no publicly
339 available datasets for this purpose. To tackle this, we gathered a large-scale dataset
340 comprising ultra-widefield images from five distinct hospital sources (Fig. 1a). We
341 sought experienced clinicians to label posterior staphyloma with binary annotations to
342 indicate its presence (NoPS or PS) and myopic maculopathy with five categories: no
343 myopic retinal lesions (NoMRL), tessellated fundus only (TFO), diffuse chorioretinal
344 atrophy (DCA), patchy chorioretinal atrophy (PCA), and macular atrophy (MA). We
345 built an end-to-end lightweight framework called RealMNet on the basis of the unified
346 platform to identify these concurrent lesions with multi-label learning (Fig. 1b). We
347 progressively determined resampling approaches (Fig. A5a), cost-sensitive calibration
348 (Fig. A4a), and classifier adaption (Fig. A4b) with the development set for mitigat-
349 ing negative impacts caused by imbalanced label distributions (Fig. 2). Hence, the
350 proposed model was functionally interpretable by identifying these clinically signifi-
351 cant lesions and objectively instrumental by alleviating multi-label imbalance issues.
352 We devised three experimental protocols (Fig. 1c) to demonstrate the model’s infer-
353 ence capacity, robustness, and generalizability. We observed that the proposed model
354 outperformed ($P < 0.001$) all other benchmark approaches (Fig. 3a). Meanwhile, our
355 model exhibited good robustness (Fig. 3b) and generalizability (Fig. 3c), even when
356 assessed on challenging subsets. For deep learning-based applications in the medi-
357 cal field, interpretability is critical when developing convincing workflows. Our model
358 exhibited good labeling efficiency, taking different ratios of training data as input
359 (Fig.). As a transformer-based architecture with hierarchical design [19], each stage
360 of RealMNet maintained helpful knowledge for lesion identification (Fig. 4b). The
361 simulated and batch-wise augmentation jointly helped the model avoid over-fitting
362 (Fig. 4c). From the heatmaps of the final results, we observed that the model’s atten-
363 tion presented a diverse region of interest for different categories. We noticed that
364 ultra-widefield images contained boundaries of physical imaging devices, which might
365 impede models from effectively capturing helpful information. We constructed the
366 dataset based on the scale of the two imaging types in the PSMM dataset (Table A3).
367 We employed ResNet-50 as the segmentation backbone and DeepLab-v3 as the seg-
368 mentation model to remove these boundaries accurately (Fig. A6a and Table A4).
369 The processed data without boundaries was then used to re-trained RealMNet with
370 processed data. Results (Fig. A6b) showed that our model was not affected by these
371 physical boundaries, demonstrating the model’s prominent capacity to capture infor-
372 mative regions. In order to verify that the developed model has a broader application
373 impact, we carried out a transfer learning on peripheral lesion discrimination, which
374 could simultaneously exist in high myopic eyes (Fig. 6a) and give rise to severe
375 visual impairment. The results (Fig. 6b) obtained from transfer learning for RealMNet
376 demonstrated promise in detecting peripheral lesions and distinguishing postoperative
377 cases (PC).

378 Although this work starts from the essential and exclusive discrimination mecha-
379 nisms of diagnosing pathologic myopia based on the workflow with deep learning, there
380 are still some limitations and challenges to address in the follow-up work. First, our
381 model cannot currently recognize “plus” lesions [30], namely, lacquer cracks, myopic

382 choroidal neovascularization, and Fuchs spot, primarily due to insufficient high-quality
383 data. Second, although our model performed well with UWF images alone, we have
384 not yet incorporated multimodal data (e.g., axial length) to improve performance fur-
385 ther. Finally, results on peripheral lesion discrimination exposed limited performance
386 on lesions with very few training data (e.g., RRD and HoT). In light of these chal-
387 lenges, we propose to gather qualified data on “plus” lesions from additional medical
388 sources and integrate clinical textual data such as axial length to improve identifica-
389 tion performance. We are optimistic that the developed model would receive excellent
390 transfer ability when pretrained on large-scale UWF images instead of natural ones.

391 In summary, we offer a dataset comprising high-quality ultra-widefield images and
392 introduce a powerful and reliable workflow for identifying clinically significant lesions
393 to aid in diagnosing pathologic myopia. Through comprehensive evaluation metrics
394 on the hand-crafted PSMM dataset, we have verified the efficacy and efficiency of
395 RealMNet relative to competitive benchmark models. RealMNet has demonstrated
396 superior robustness and generalizability, offering novel perspectives for deep learning-
397 based fine-grained clinical decisions.

398 4 Methods

399 4.1 Dataset construction

400 We show details about the course of data acquisition and labeling. We perform essential
401 data processing and stratified data partitioning to facilitate model training.

402 4.1.1 Acquisition and labeling

403 The PSMM dataset consisted of five sub-sources: ShenzhenEye, SUSTech, LishuiR,
404 Zhongshan, and LishuiZ. The ShenzhenEye subset contained 38,922 UWF images of
405 4,003 patients collected from Shenzhen Eye Hospital of China between January 1st,
406 2019 and December 31st, 2023. The SUSTech subset contained 2,835 UWF images of
407 226 patients collected from the Southern University of Science and Technology Hos-
408 pital of China between January 1st, 2023 and June 31st, 2023. The LishuiR subset
409 contained 938 UWF images of 155 patients collected from Lishui People’s Hospital
410 of China between January 1st, 2021 and December 31st, 2023. The Zhongshan subset
411 contained 456 UWF images of 85 patients collected from Zhongshan Ophthalmic Cen-
412 ter, Sun Yat-sen University of China. The LishuiZ subset contained 220 UWF images
413 of 91 patients collected from Lishui Central Hospital of China between January 1st,
414 2021 and December 31st, 2023. Ultimately, we integrated these resources to estab-
415 lish the PSMM dataset that contained 43,371 UWF images of 4,560 patients. Two
416 UWF scanning laser ophthalmoscopy imaging devices captured these images, Day-
417 tona (P200T) and California (P200DTx). We retrieved these images by the keywords
418 of *{High Myopia, Pathologic Myopia}*. We were prone to partially retrieve severe sam-
419 ples from the hospital to form the Zhongshan subset as a challenging subset. Fewer
420 samples were collected in the LishuiR and LishuiZ subsets due to certain limitations
421 in the medical record management of the two hospitals, despite retrieving them over

422 a long period. The ShenzhenEye subset naturally served as the main subset in pro-
423 portion, and the other fours as auxiliary subsets. Two junior clinicians labeled these
424 UWF images, and one senior clinician then double-checked the labeled images by dis-
425 carding distorted or damaged images for rigorous quality assurance. The composition
426 of the hand-crafted PSMM dataset and its integral subsets are presented in Table A1.

427 **4.1.2 Data processing and stratified partition**

428 We desensitized all the data to prevent privacy exposure. We centralized the objec-
429 tive (photographing area) by removing futile black outer boundaries and then resized
430 images beforehand to facilitate model training. For ease of application and adapta-
431 tion, we structured the dataset following the format of the PASCAL Visual Object
432 Classes Challenge (PASCAL VOC) 2007 dataset [31], which is a well-known dataset
433 in the computer vision field developed to recognize objects in realistic scenes. Due to
434 a limited amount of data, an increasing number of published methods are trained on
435 the training set and evaluated on the testing set directly to showcase optimal perfor-
436 mance presentation regardless of fair comparison. However, in real-world scenarios,
437 researchers need to develop reliable methods in various situations. This means it is
438 crucial to evaluate these methods on a separate development set for convincing model
439 validation. In order to support our claim, we divided the PSMM dataset into three
440 separate parts: training, development, and testing sets with a distribution of 7:1.5:1.5.
441 This allowed us to assess the research using the development set and then finalize the
442 method and evaluate it using the unseen testing set. While dividing data into different
443 sets is common in deep learning tasks, it becomes more complex when dealing with the
444 clinical challenge presented in this study. Notably, each patient typically has multiple
445 UWF images, which can occur in two scenarios: multiple images are taken in a single
446 examination to ensure an accurate diagnosis, or images are taken at different times
447 during multiple examinations. To ensure reliable photography, several UWF images
448 are captured at the same time for each patient, and many patients undergo examina-
449 tions at different times. As a result, it's not feasible to split UWF images from the same
450 patient into different sets during data partitioning. Furthermore, as mentioned earlier,
451 our objective involves a multi-label learning task, which further complicates the data
452 partitioning process. To address this, we adopted an approach where we assigned a
453 single-class label for each patient and employed a stratified strategy to ensure indepen-
454 dent and identically distributed partitioning [32]. Specifically, we assigned a pseudo
455 single-class label that was quantitatively dominant over all labels of UWF images for
456 each patient and then stratified the patient image groups into training, development,
457 and testing sets.

458 **4.2 End-to-end lightweight hybrid framework**

459 We present details about the feature extraction backbone and optimized designs
460 with cost-sensitive calibration and classifier adaptation for multi-label imbalance
461 alleviation.

462 **4.2.1 Lightweight pretraining distillation backbone**

463 We harness TinyViT [15] as the fundamental backbone to ensure the model achieves
464 excellent performance while retaining lightweight. TinyViT is favored for its applica-
465 tion of distillation during pretraining for knowledge transfer. We employ a hierarchical
466 design to address the need for multi-scale features in identifying pathological pat-
467 terns. This architecture comprises four stages, each featuring a gradual reduction in
468 resolution akin to the Swin Transformer [19] and LeViT [33]. The patch embedding
469 block incorporates two convolutions with a 3x3 kernel, a stride of 2, and a padding
470 of 1. In the initial stage, we implement lightweight and efficient MBCOnvs [34] and
471 downsampling blocks, recognizing that convolutions at earlier layers can proficiently
472 learn low-level representations due to their strong inductive biases. The subsequent
473 three stages are constructed with transformer blocks, leveraging window attention to
474 mitigate computational costs. To capture local information, we introduce attention
475 biases and a 3x3 depth-wise convolution between attention and MLP. Each block in
476 the initial stage, as well as attention and MLP blocks, is complemented by a residual
477 connection. The activation functions adhere to the GELU model, and the normal-
478 ization layers for convolution and linear operations are BatchNorm and LayerNorm,
479 respectively. The embedded dimensions in each stage of the adopted backbone are 96,
480 192, 384, and 576. Furthermore, the number of blocks in each stage of the backbone
481 corresponds to that of Swin-T: 2, 2, 6, and 2.

482 **4.2.2 Cost-sensitive calibration**

483 Cost-sensitive methods are practical and efficient techniques that take into account
484 the costs resulting from prediction mistakes made by the model. When dealing with
485 the complication of lesions in terms of posterior staphyloma and myopic maculopathy,
486 we aim to explore cost-sensitive approaches suitable for multi-label learning. We begin
487 by using the Binary Cross-Entropy (BCE) Loss, based on cross-entropy in information
488 theory. In this context, cross-entropy of the distribution q relative to a distribution p
489 over a given set is defined as follows:

$$\mathcal{H}(p, q) = -\mathbb{E}_p[\log q]$$

490 where $\mathbb{E}_p[\cdot]$ is the expected value operator regarding the distribution p . Cross-entropy
491 can be utilized to create a loss function in machine learning and optimization:

$$\mathcal{H}(p, q) = - \sum_i p_i \log q_i = -[y \log \hat{y} + (1 - y) \log (1 - \hat{y})]$$

492 where y means the ground-truth and \hat{y} means the predictions from the model. Next,
493 we introduce a weight factor $\alpha \in [0, 1]$ to help tackle class imbalance and a modulating
494 factor $(1 - p)^\gamma$ to reshape the loss function, thereby reducing the emphasis on easy
495 examples and focusing training on challenging negatives [22]. Till now, we define the
496 cost-sensitive calibration (CSC) as follows:

$$CSC = -\alpha [p^\gamma \log p + (1 - p)^\gamma \log (1 - p)]$$

497 where $p = \sigma(z)$ is the prediction probability given output logits z and γ is the focusing
 498 parameter. We also separate the focusing levels of positive and negative samples to
 499 avoid eliminating gradients from rare positive samples when setting a high value for
 500 γ . Additionally, we examine the effects of asymmetric probability shifting, achieved
 501 by setting a probability margin $m \geq 0$ to reject mislabeled negative samples [23].
 502 Therefore, the ultimate CSC is defined as follows:

$$CSC = -\alpha [(p_m)^{\gamma_-} \log p + (1-p)^{\gamma_+} \log (1-p)]$$

503 where $p_m = \max(p - m, 0)$ is the shifted probability, γ_+ and γ_- are positive and
 504 negative focusing parameters, respectively. Furthermore, we evaluate the effectiveness
 505 of a state-of-the-art cost-sensitive method called Two-way Loss [24], specially designed
 506 for multi-label learning. We follow the original computational formula:

$$\ell = \text{softplus} \left[T_{\mathcal{N}} \log \sum_{n \in \mathcal{N}} e^{\frac{x_n}{T_{\mathcal{N}}}} + T_{\mathcal{P}} \log \sum_{p \in \mathcal{P}} e^{-\frac{x_p}{T_{\mathcal{P}}}} \right]$$

507 where $\text{softplus}(\cdot) = \log[1 + \exp(\cdot)]$, \mathcal{P} means positive labels, \mathcal{N} means negative labels,
 508 $T_{\mathcal{N}}$ and $T_{\mathcal{P}}$ are two temperatures applied to negative and positive logits, respectively.
 509 We fine-tune temperature parameters through grid search for optimal performance.

510 4.2.3 Classifier adaptation

511 Classifier adaptation is technically complex but helpful for addressing multi-label
 512 imbalance issues by adjusting the model's classifier design. The design of the imple-
 513 mented classifier is inspired by a simple and efficient module called class-specific
 514 residual attention [25] that achieves state-of-the-art results on multi-label recognition.

515 Given an input image \mathcal{I} with the scale of $H \times W$, the backbone as a feature extractor
 516 \mathcal{F} transforms the input image into a feature tensor $\mathbf{x} \in \mathbb{R}^{d \times h \times w}$ by $\mathbf{x} = \mathcal{F}(\mathcal{I}; \theta)$,
 517 where θ represents parameters of the backbone. The feature tensor is decoupled as
 518 $\mathbf{x}_1, \mathbf{x}_2, \dots, \mathbf{x}_P$, where $\mathbf{x}_p \in \mathbb{R}^d$ indicates the p -th feature tensor in positions $P = h \times w$.

519 The class-specific attention scores are presented by $s_p^i = \frac{\exp(\mathcal{T} \mathbf{x}_p^\top \mathbf{c}_i)}{\sum_{i=1}^P \exp(\mathcal{T} \mathbf{x}_p^\top \mathbf{c}_i)}$, where Here,
 520 s_p^i can be regarded as the probability of i -th class appearing at the position p with
 521 $\sum_{p=1}^P s_p^i = 1$ and \mathcal{T} stands for the temperature controlling the sharpness of the scores.
 522 The class-specific feature vector for i -th class is $\mathbf{v}_{spec}^i = \sum_{p=1}^P s_p^i \mathbf{x}_p$. The class-agnostic
 523 feature vector for the entire image is $\mathbf{v}_{agno} = \frac{1}{P} \sum_p \mathbf{x}_p$. The final feature vector for
 524 the i -th class is $\mathbf{v}^i = \mathbf{v}_{agno} + \lambda \mathbf{v}_{spec}^i$. The classifier produces $\hat{\mathbf{y}} \triangleq (y^1, y^2, \dots, y^n) =$
 525 $(\mathbf{c}_1^\top \mathbf{v}^1, \mathbf{c}_2^\top \mathbf{v}^2, \dots, \mathbf{c}_n^\top \mathbf{v}^n)$, where n stands for the number of classes. The final prediction
 526 is produced with multi-head extension to the residual attention by $\hat{\mathbf{y}} = \sum_{h=1}^H \hat{\mathbf{y}}_{\mathcal{T}_h}$,
 527 where $\hat{\mathbf{y}}_{\mathcal{T}_h} \in \mathbb{R}^n$ represents the logits of head h .

528 **4.3 Experimental protocols**

529 We introduced three distinct experiment protocols that naturally empowered both the
530 internal and external validation of the model, quantitatively demonstrating that the
531 proposed model was efficient with good robustness and generalizability.

532 **4.3.1 Centralized inference**

533 The centralized inference protocol aimed to demonstrate the inference capacity of
534 models directly on the intact PSMM dataset. Models were trained on the training set of
535 the PSMM dataset and tested on the testing set of the PSMM dataset. Models learned
536 task-specific knowledge from all available training resources and were developed on
537 the development set of the PSMM dataset, eventually inferring all available unseen
538 testing resources. In our experiments, we compared our method, RealMNet, with four
539 widely recognized models under the centralized inference protocol, in which models
540 were sufficiently motivated for optimal identification performance.

541 **4.3.2 Main-source robustness**

542 The main-source robustness protocol aimed to demonstrate the robustness of models
543 on the separate PSMM dataset. Models were trained solely on the main subset and
544 tested on four auxiliary subsets, the averaged performances of which were provided.
545 All data from the main-source dataset comprised the training set, and each auxiliary-
546 center dataset served as the testing set separately. In our experiments, we implemented
547 our method, RealMNet, under the main-source robustness protocol for robustness
548 verification.

549 **4.3.3 Cyclic-source generalization**

550 The cyclic-source generalizability protocol aimed to demonstrate the generalizability
551 of models on the separate PSMM dataset. Models were trained on the main-source
552 dataset combined with three auxiliary-center datasets and tested on the rest of the
553 auxiliary dataset. The performances of four cyclic experiments were provided. In
554 our experiments, we implemented our method, RealMNet, under the cyclic-source
555 generalizability protocol for generalization verification.

556 **4.4 Evaluation metrics**

557 Cutting-edge artificial intelligence models frequently excel based on a single or a few
558 evaluation metrics. However, this can introduce bias into the results and impact the
559 perception of their scientific objectivity [35]. This issue is particularly relevant in multi-
560 label learning, which is more intricate than single- and multi-class learning [36]. In our
561 study, we opted for comprehensive measures to assess both bipartitions and rankings,
562 considering the characteristics of multi-label data [37].

563 Considering a development set that has multi-label samples $(\mathbf{x}_i, \mathbf{y}_i)$ where $i =$
564 $1, \dots, N$ and N means the number of samples. The labelset of i -th sample $\mathbf{y}_i \subseteq \mathcal{L}$
565 where $\mathcal{L} = \{\lambda_l : j = 1, \dots, L\}$ is the set of all ground-truth labels and L means the
566 number of labels. For each label λ , the rank is termed as $r_i(\lambda)$. The predictions made

567 by the Multi-Label Classifier (MLC) are defined as $\hat{\mathbf{y}}_i$. Let $tp_\lambda, fp_\lambda, tn_\lambda$, and fn_λ be
 568 the number of true positives, false positives, true negatives, and false negatives after
 569 binary evaluation for a label λ .

570 For the evaluation of bipartitions, we use Precision = $\frac{tp}{tp+fp}$ to reflect the ability
 571 not to label as positive a sample that is negative. We use Recall = $\frac{tp}{tp+fn}$ (also called
 572 Sensitivity) to reflect the ability to find all positive samples. A good discrimination
 573 model should be sensitive in identifying as many potential positive samples as possi-
 574 ble to help screen in medical scenarios. The F-measure is the harmonic mean of the
 575 Precision and Recall that symmetrically represents Precision and Recall in one met-
 576 ric. We use F1 Score = $\frac{2\text{Precision} \times \text{Recall}}{\text{Precision} + \text{Recall}}$ to reveal the balanced ability of the model to
 577 both capture positive cases (Recall) and be accurate with the cases it does capture
 578 (Precision), which is exceptionally able to measure performance objectively when the
 579 class balance is skewed. We use mean Average Precision (mAP) to reflect the aver-
 580 age fraction of relevant labels ranked higher than one other relevant label, which is
 581 calculated by:

$$\text{mAP} = \frac{1}{L} \sum_{\lambda=1}^L \sum_n (R_n - R_{n-1}) P_n$$

582 where R_n and P_n stand for Precision and Recall at the n -th threshold, respectively.
 583 The AUROC (Area Under the Receiver Operating Characteristic Curve) indicates the
 584 level of separability of a model. This metric is calculated as the area under the Receiver
 585 Operating Characteristic Curve (ROC). A larger AUROC indicates that the model can
 586 achieve a high true positive rate while maintaining a low false positive rate. Essentially,
 587 it demonstrates the model's ability to differentiate between classes. The measures
 588 above can be calculated using two types of averaging operations: macro-averaging and
 589 micro-averaging. Specifically, given a bipartition-based measure \mathcal{B} ,

$$\begin{aligned} \mathcal{B}_{\text{macro}} &= \frac{1}{L} \sum_{\lambda=1}^L \mathcal{B}(tp_\lambda, fp_\lambda, tn_\lambda, fn_\lambda) \\ \mathcal{B}_{\text{micro}} &= \mathcal{B}\left(\sum_{\lambda=1}^L tp_\lambda, \sum_{\lambda=1}^L fp_\lambda, \sum_{\lambda=1}^L tn_\lambda, \sum_{\lambda=1}^L fn_\lambda\right) \end{aligned}$$

590 We do not use popular Accuracy as an evaluation metric, which overestimates models
 591 that only predict well for the majority class by simplistically measuring the absolute
 592 amount of correct predictions. We use Hamming Loss to measure the proportion of
 593 incorrectly classified instance-label pairs, which is defined as follows:

$$\text{Hamming Loss} = \frac{1}{NL} \sum_{i=1}^N |\mathbf{y}_i \neq \hat{\mathbf{y}}_i|$$

594 For the evaluation of rankings, we use Coverage to assess the average number of
 595 steps required to encompass all relevant labels in the ranked label list for each example,

596 which is defined as follows:

$$\text{Coverage} = \frac{1}{N} \sum_{i=1}^N \max_{\lambda \in \mathbf{y}_i} r_i(\lambda) - 1$$

597 We use Ranking Loss to evaluate the fraction of reversely ordered label pairs, which
598 is defined as follows:

$$\text{Ranking Loss} = \frac{1}{N|\mathbf{y}_i||\overline{\mathbf{y}}_i|} \sum_{i=1}^N |\{(\lambda_a, \lambda_b) : r_i(\lambda_a) > r_i(\lambda_b), (\lambda_a, \lambda_b) \in \mathbf{y}_i \times \overline{\mathbf{y}}_i\}|$$

599 where $\overline{\mathbf{y}}_i$ is the complementary set of \mathbf{y}_i with respect to \mathcal{L} .

600 4.5 Implementation details

601 4.5.1 Benchmark approaches

602 Our model retained lightweight thanks to pretraining distillation techniques and
603 leveraged hierarchical transformer architectures that incorporated convolution opera-
604 tions. Therefore, we selected various widely used benchmark counterparts: DeiT [16],
605 ConvNeXt [18], EfficientNet [17], and Swin Tranformer [19]. Specifically, DeiT is a
606 convolution-free transformer trained with a distillation procedure. ConvNeXt is a pure
607 ConvNet that is modernized toward the design of a vision transformer. EfficientNet is
608 a ConvNet designed using neural architecture search to enable model scaling with sig-
609 nificantly fewer parameters. Swin Transformer is a hierarchical transformer that can
610 be modeled at various scales. We compare RealMNet to these benchmark approaches
611 with respect to model development in Table 4.

612 4.5.2 Training and testing

613 We approached the problem in this study as a multi-label learning task to account
614 for the complex relationships between pathological patterns and explore their under-
615 lying interdependencies. We chose TinyViT-21m as the feature extractor backbone
616 of RealMNet and initialized it with weights pretrained on ImageNet-21k using pre-
617 training distillation. The image size was set at 384×384 for model development and
618 512×512 for optimal performance. The model was optimized using Adam with decou-
619 pled weight decay (AdamW) [38] with an initial learning rate of 1e-4 and a weight
620 decay of 0.05, trained with a batch size of 16 per graphics processing unit. We imple-
621 mented warmup for 10% of the total 50 epochs, with a starting factor of 1e-2, followed
622 by a cosine annealing schedule with a learning rate of 1e-6. A drop path rate of 0.5
623 was used to prevent over-fitting. We employed two types of augmentation techniques:
624 simulated and batch-wise. Simulated augmentation was intended to mirror real-world
625 scenarios by means of spatial-level and pixel-level transformation. For spatial-level
626 transformation, we used a random affine, random flip, and random erasing. For pixel-
627 level transformation, we used a Gaussian blur, Gauss noise, and Color jitter. The
628 batch-wise transformation involved Mixup [39] and CutMix [40]. For simplicity, we

629 used the same parameter settings as in the previous study [32] for UWF images. We
630 leveraged asymmetric focusing as a cost-sensitive calibration with tunable parameters
631 ($\gamma_+ = 3$ and $\gamma_- = 4$). We harnessed classifier adaptation with the leveraging parame-
632 ter $\lambda = 1.2$ and $H = 2$ multi-head attention. In the centralized inference protocol, the
633 entire PSMM dataset is divided into a training set, a development set, and a test set
634 at a ratio of 7:1.5:1.5 using stratified partitioning. In the main-source robustness pro-
635 tocol, the ShenzhenEye subset is utilized as the training set, while the remaining four
636 source subsets take turns as the test set. In the cyclic-source generalizability protocol,
637 the ShenzhenEye subset and three of the remaining four sources are used as the train-
638 ing set, and testing is conducted on the subset of the last source. In all experimental
639 protocols, the ML-RUS [41] resampling method was applied to the training set only,
640 with an undersampling ratio of 0.2. Experiments were deterministic and reproducible,
641 with a fixed seed of 42. We conducted the training and testing on the OpenMMLab
642 platform using 4 NVIDIA GeForce RTX 4090 GPUs.

643 4.6 Extensibility

644 4.6.1 Broader impact statement

645 The inherent patterns of the model developed in this study make it easy to use for
646 tasks concerning concurrent lesion identification. In this study, we emphasized the sig-
647 nificance of identifying peripheral retinal lesions in highly myopic eyes. To resolve this
648 challenge, we employed our model by initializing the backbone with weights trained on
649 the PSMM dataset and then fine-tuning the model on data specific to peripheral reti-
650 nal lesions. We observed that the fine-tuned model generally performed well, with an
651 AUROC of 0.8642 (95% CI 0.8405-0.8880) in discerning concurrent peripheral retinal
652 regions with the proposed off-the-shelf workflow without bells and whistles. We found
653 that the fine-tuned model could accurately perceive postoperative cases (PC) with an
654 F1 Score of 0.8394 (95% CI 0.8033-0.8754), mAP of 0.8894 (95% CI 0.8580-0.9208),
655 and AUROC of 0.9029 (95% CI 0.8721-0.9336). We inferred an inferior capacity to dis-
656 tinguish rhegmatogenous retinal detachment (RRD) and holes or tears (HoT), possibly
657 due to the scarcity of real-world data. Notably, we used consistent training settings for
658 the intuitive perception of transfer capacity, which signified the potential for improved
659 performance with further investigation. The success of our workflow in identifying
660 peripheral retinal lesions highlights its broader utility for enhancing the diagnosis of
661 retinal diseases and other complex medical scenarios.

662 **Acknowledgements.** We thank the support from the National Natural Sci-
663 ence Foundation of China 32350410397; Science, Technology, Innovation Commis-
664 sion of Shenzhen Municipality, JCYJ20220530143014032, JCYJ20230807113017035,
665 KCXFZ20211020163813019, Shenzhen Medical Research Funds, D2301002; Depart-
666 ment of Chemical Engineering-iBHE special cooperation joint fund project, DCE-
667 iBHE-2022-3; Tsinghua Shenzhen International Graduate School Cross-disciplinary
668 Research and Innovation Fund Research Plan, JC2022009; and Bureau of Planning,
669 Land and Resources of Shenzhen Municipality (2022) 207.

670 **Declarations**

671 **4.7 Competing interests**

672 The authors declare no competing interests.

673 **4.8 Ethics approval**

674 The study followed the guidelines of the World Medical Association Declaration of
675 Helsinki 1964, updated in October 2013, and was conducted after approval by the
676 Ethics Committees of Shenzhen Eye Hospital (2023KYPJ087).

677 **4.9 Reporting summary**

678 Further information on research design is available in the Nature Portfolio Reporting
679 Summary linked to this article.

680 **4.10 Data availability**

681 All benchmark datasets we assembled are publicly available at Zenodo/GitHub/-
682 figshare/Kaggle (choose the optimal alternative).

683 **4.11 Code availability**

684 The codes and trained models developed for this study are publicly available at
685 <https://github.com/yo3nglau> (updated with the particular project website). Label-
686 ing was completed with the open-source graphical image annotation software labelme
687 v5.3.1 (<https://github.com/labelmeai/labelme>). The code is built on three open-
688 source projects, MMCV v2.0.1, MMEngine v0.8.4, and MMPREtrain v1.0.2 of the
689 OpenMMLab codebase (<https://github.com/open-mmlab>). The evaluation metrics are
690 implemented with scikit-learn v1.3.2 (<https://github.com/scikit-learn/scikit-learn>).
691 All experiments are supervised on Weights & Biases v0.16.4 ([https://github.com/
692 wandb/wandb](https://github.com/wandb/wandb)). All histograms and line charts are drawn by Matplotlib v3.9.1
693 (<https://github.com/matplotlib/matplotlib>). The Sankey map and Chord diagram are
694 drawn by Plotly v5.22.0 (<https://github.com/plotly/plotly.py>) and pyCirclize v1.6.0
695 (<https://github.com/moshi4/pyCirclize>), respectively.

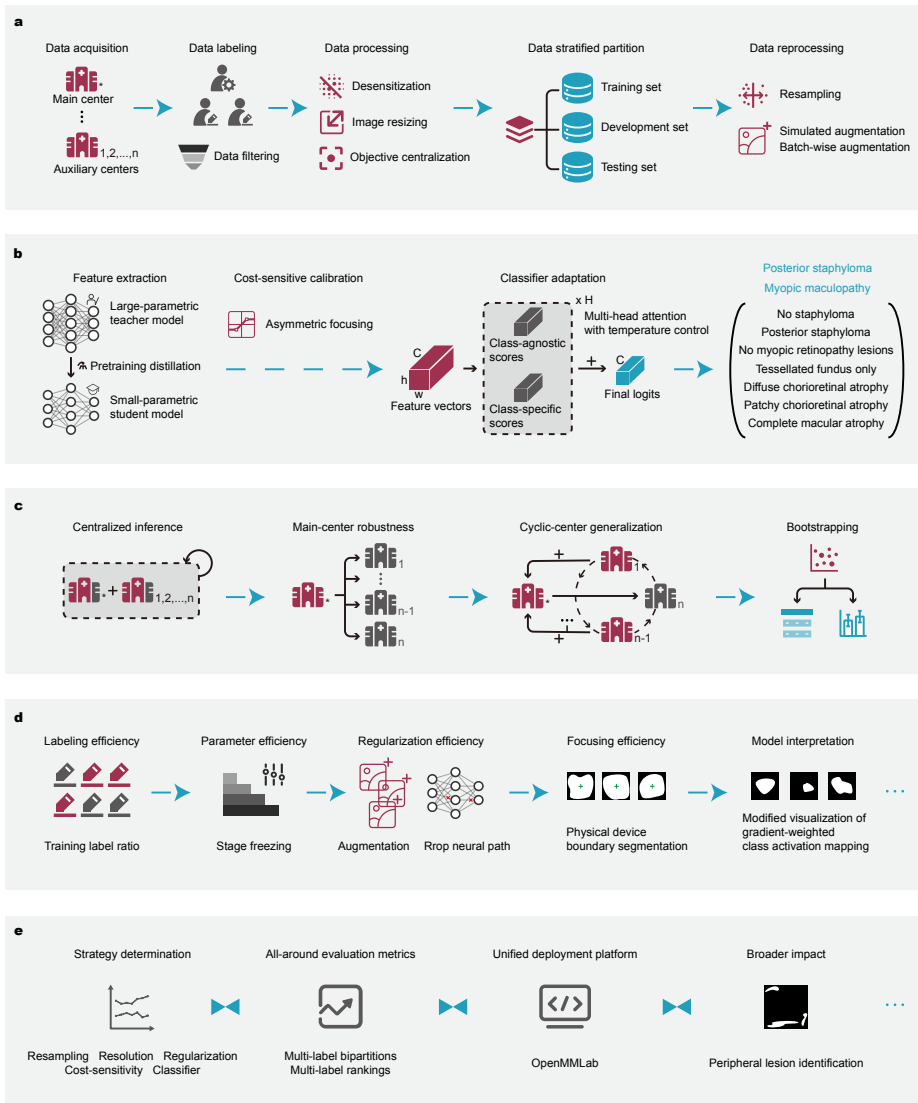


Fig. 1: General overview of the study. **a**, Data machining: data are collected from one main center and four auxiliary centers. After double-checking labeling, quality filtering, and essential processing, a stratified partition is implemented to ensure that the distribution of lesions remains similar across sets. Resampling and augmentation techniques are then used to alleviate label imbalance. **b**, Model training and inference: the pretraining-distilled small parametric model is task-specifically fine-tuned with asymmetric focusing and classifier adaptation, which complementally mitigate label imbalance. **c**, Experimental protocols: three protocols are designed to demonstrate precise inference, robustness, and generalizability of the proposed method. All experiments are implemented by bootstrapping the testing set 1,000 times. **d**, Interpretable workflow: Model efficiencies of dataset labeling, training parameters, regularization techniques, and focusing regions are extensively examined. Visualizations of gradient-weighted class activation mapping are provided for intuitive interpretations. **e**, Model development and assessment: Models are progressively developed through strategy determination, and their performance is assessed on a unified deployment platform using all-around evaluation metrics.

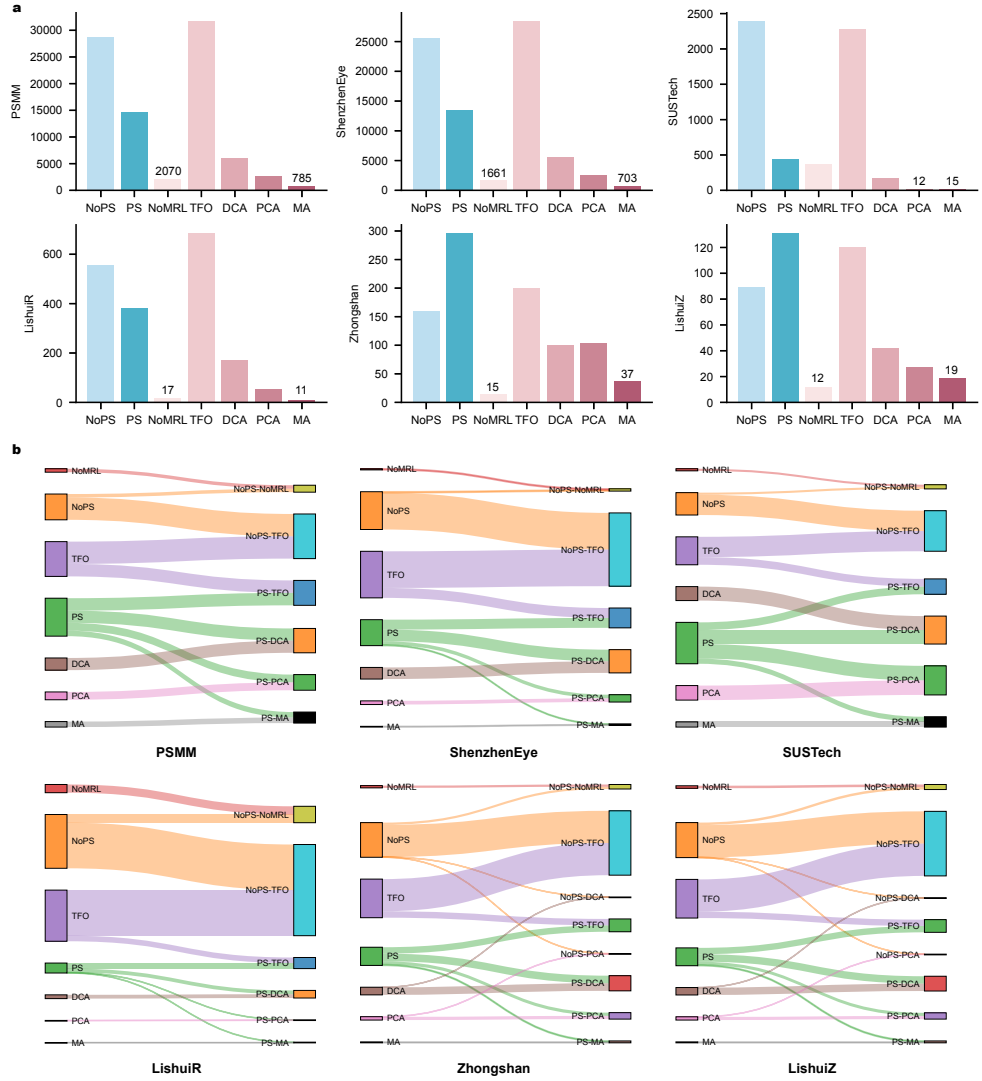


Fig. 2: Statistics and complications associated with lesions of posterior staphyloma and myopic maculopathy. **a**, Statistical analysis of the seven categories in the PSMM dataset and its subsets, with specific values assigned to the minimum two categories of each dataset. **b**, Illustrations of complications arising from posterior staphyloma and myopic maculopathy. Sankey diagrams are plotted to illustrate the distribution of these complications in the PSMM dataset and its subsets.

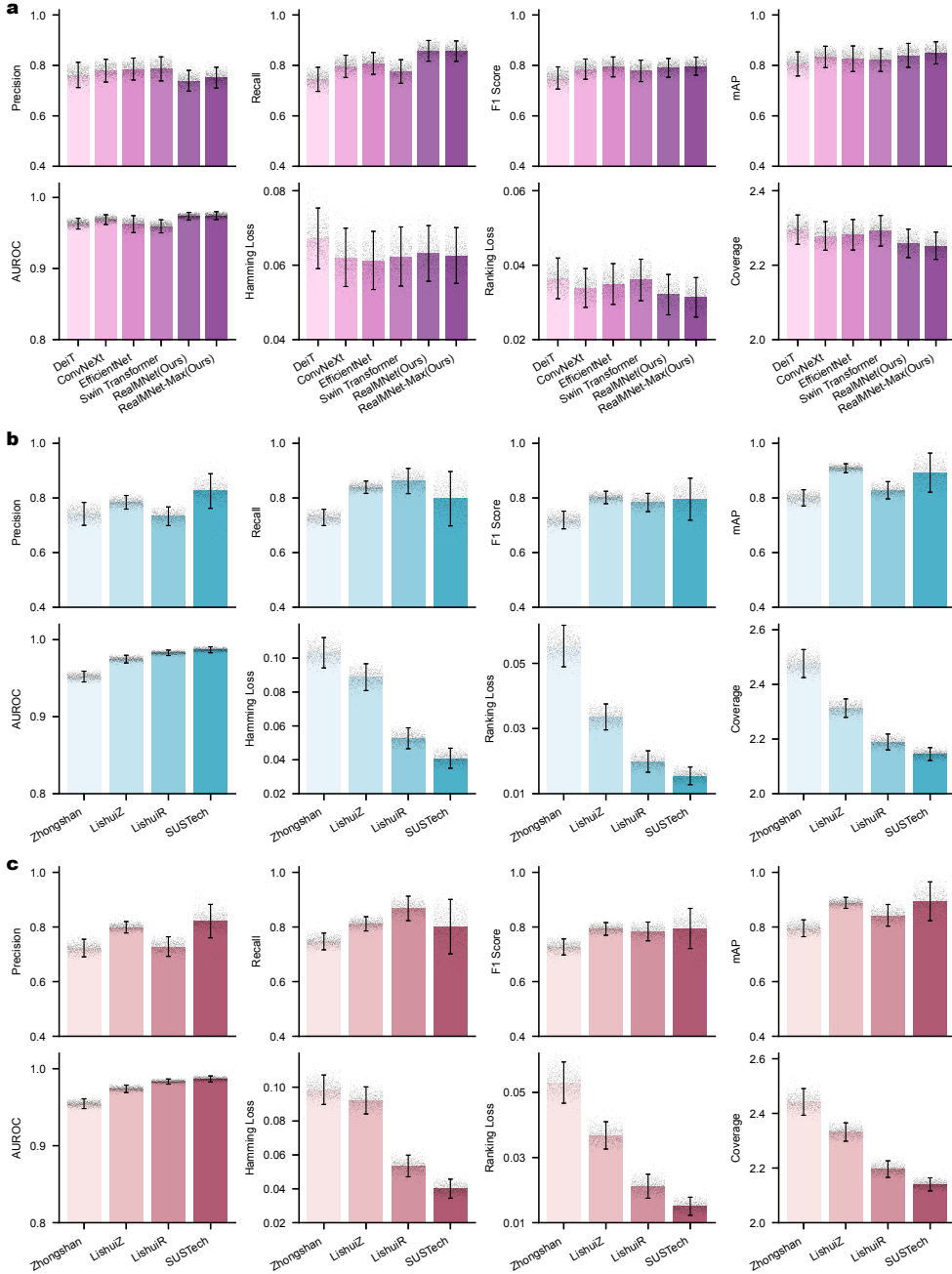


Fig. 3: Model performance under three experimental protocols. **a**, Evaluating model inference capability using the centralized inference protocol. The proposed models are compared to four well-known benchmarks: DeiT, ConvNeXt, EfficientNet, and Swin Transformer. **b**, Assessing model robustness by training on the main source subset and testing on four auxiliary source subsets under the main-source robustness protocol. **c**, Assessing model generalizability by training on the main source subset combined with three of the four auxiliary source subsets and testing on the remaining subset under the cyclic-source generalizability protocol. The error bars represent the 95% confidence interval (CI) of the estimates, and the bar center represents the mean estimate of the displayed metric. The estimates are computed by generating a bootstrap distribution with 1,000 bootstrap samples for corresponding testing sets with $n=1,000$ samples.

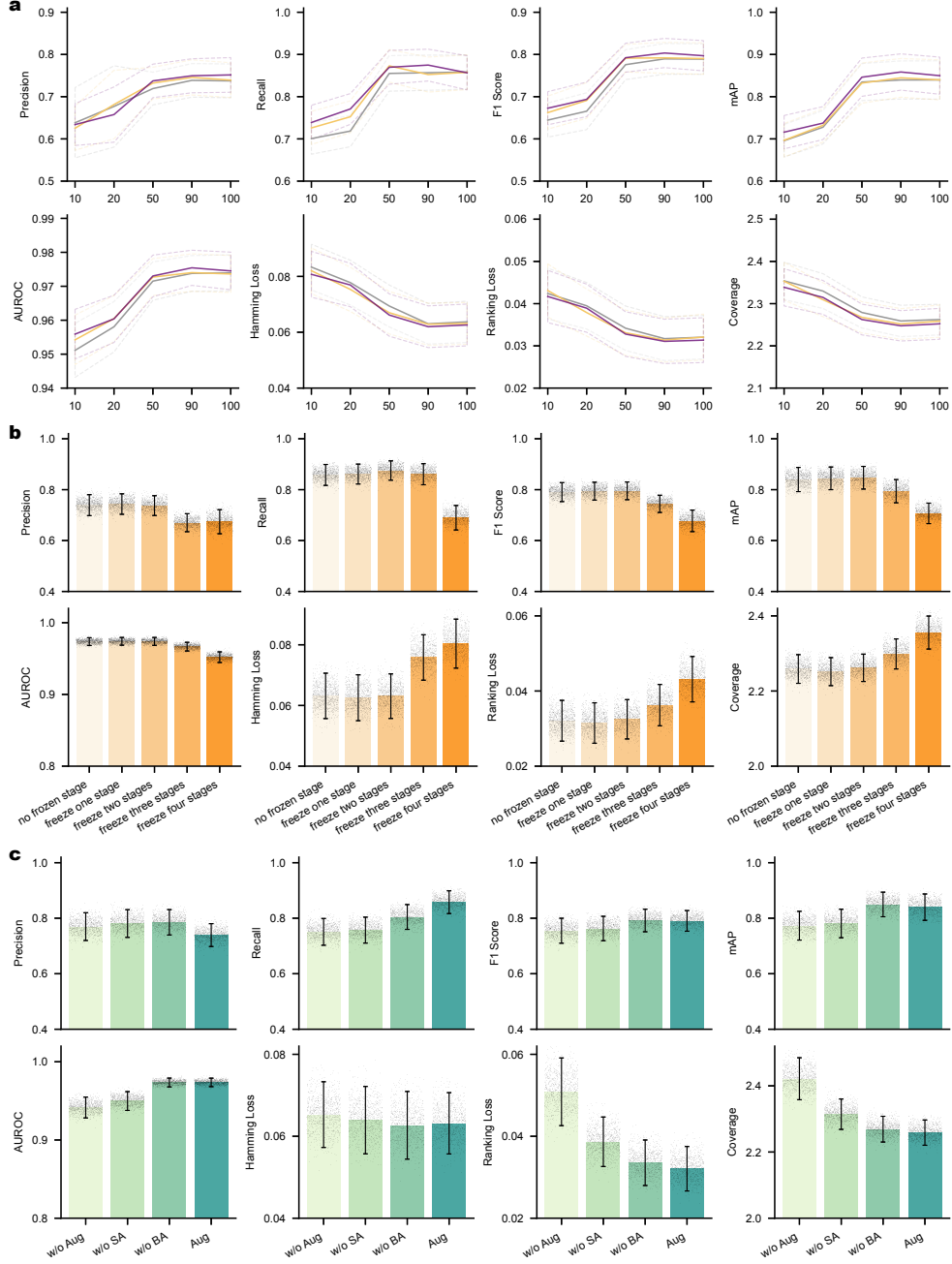


Fig. 4: Efficiency of RealMNet in identifying posterior staphyloma and myopic maculopathy on the PSMM dataset. **a**, Labeling efficiency: we progressively increase the amount of training data and labels to achieve precise and stable performance. The 95% confidence interval (CI) of the displayed metrics are plotted in dotted lines, and the central lines indicate the mean value. **b**, Parameter efficiency: we freeze training parameters from different stages to observe the contribution of each stage. **c**, Augmentation efficiency: We ablate two types of augmentation techniques, namely simulated augmentation (SA) and batch-wise augmentation (BA), to observe the performance gains that RealMNet gets as a result of these techniques. The error bars represent 95% CI of the estimates, and the bar center represents the mean estimate of the displayed metric. The estimates are computed by generating a bootstrap distribution with 1,000 bootstrap samples for corresponding testing sets with $n=1,000$ samples.

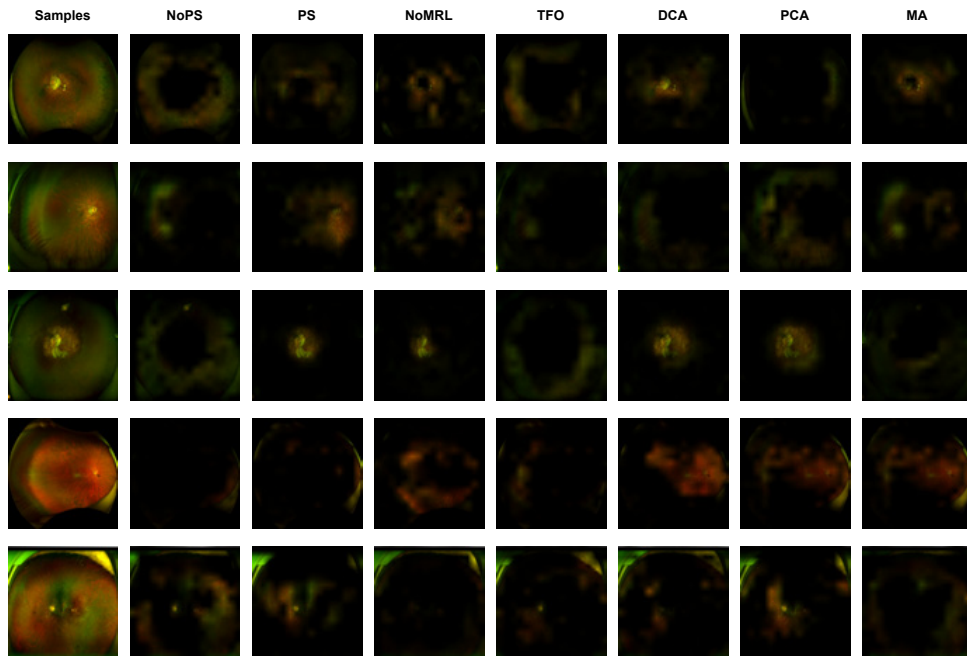


Fig. 5: We generated visualizations using an improved version of gradient-weighted class activation mapping (Grad-CAM++). These visualizations show the predictions of RealMNet for each category of posterior staphyloma and myopic maculopathy. By merging the heatmaps with the original images, we highlight the dispersed regions that are associated with lesions related to posterior staphyloma and myopic maculopathy.

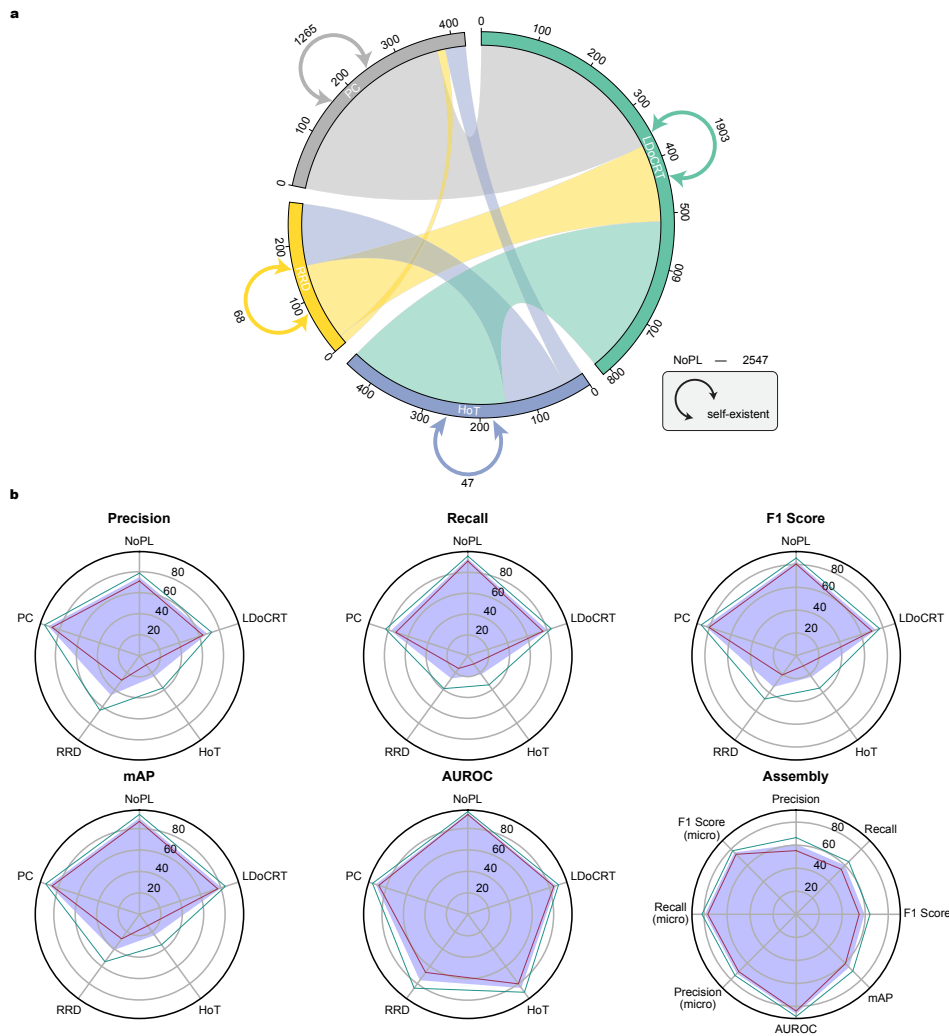


Fig. 6: Identifying complicated peripheral lesions. **a**, Concurrent distribution of peripheral lesions. Peripheral lesions may have different concurrent relationships with each other, or they may occur separately. **b**, Model performance on peripheral lesion identification. The blue facecolor represents the mean of the results, and the green outer and red inner boundaries represent the upper and lower bounds of the 95% confidence interval, respectively. All radar plots display class-wise performance on specific metrics, with the last radar plot representing the average performance on all evaluated metrics.

Table 1: Model class-wise performance on the evaluation metric of F1 Score.

Model	NoPS	PS	NoMRL	TFO	DCA	PCA	MA
DeiT	92.9080±0.0220	84.9378±0.0465	65.8115±0.1929	93.1385±0.0216	64.9436±0.1112	64.0049±0.1537	59.4071±0.3663
ConvNeXt	93.4954±0.0216	86.6145±0.0443	67.4836±0.1821	93.3462±0.0205	69.4887±0.1009	69.1593±0.1467	70.0695±0.3148
EfficientNet	93.3104±0.0220	86.3812±0.0440	67.8674±0.1824	93.4917±0.0202	68.5025±0.1026	74.8105±0.1361	71.4768±0.3003
Swin Transformer	93.2645±0.0213	85.9297±0.0436	64.8995±0.2008	93.6117±0.0207	69.4373±0.1047	67.9535±0.1534	69.7311±0.3287
RealMNet(Ours)	93.7815±0.0208	86.6268±0.0427	68.8711±0.1658	93.5031±0.0209	71.4770±0.0929	72.1523±0.1373	66.7895±0.3134
RealMNet-Max(Ours)	93.8404±0.0204	86.2816±0.0427	70.5547±0.1658	93.5852±0.0206	71.8504±0.0909	72.2685±0.1367	69.5145±0.3117

Table 2: Model class-wise performance on the evaluation metric of mAP.

Model	NoPS	PS	NoMRL	TFO	DCA	PCA	MA
DeiT	92.9080±0.0220	84.9378±0.0465	65.8115±0.1929	93.1385±0.0216	64.9436±0.1112	64.0049±0.1537	59.4071±0.3663
ConvNeXt	93.4954±0.0216	86.6145±0.0443	67.4836±0.1821	93.3462±0.0205	69.4887±0.1009	69.1593±0.1467	70.0695±0.3148
EfficientNet	93.3104±0.0220	86.3812±0.0440	67.8674±0.1824	93.4917±0.0202	68.5025±0.1026	74.8105±0.1361	71.4768±0.3003
Swin Transformer	93.2645±0.0213	85.9297±0.0436	64.8995±0.2008	93.6117±0.0207	69.4373±0.1047	67.9535±0.1534	69.7311±0.3287
RealMNet(Ours)	98.7762±0.0063	93.3474±0.0390	76.8974±0.1809	98.7188±0.0071	76.2035±0.1202	74.0739±0.1749	69.8559±0.4057
RealMNet-Max(Ours)	98.7822±0.0063	93.0462±0.0432	78.0920±0.1822	98.7352±0.0072	75.7264±0.1222	76.1924±0.1705	74.2466±0.3623

Table 3: Model class-wise performance on the evaluation metric of AUROC.

Model	NoPS	PS	NoMRL	TFO	DCA	PCA	MA
DeiT	92.9080±0.0220	84.9378±0.0465	65.8115±0.1929	93.1385±0.0216	64.9436±0.1112	64.0049±0.1537	59.4071±0.3663
ConvNeXt	93.4954±0.0216	86.6145±0.0443	67.4836±0.1821	93.3462±0.0205	69.4887±0.1009	69.1593±0.1467	70.0695±0.3148
EfficientNet	93.3104±0.0220	86.3812±0.0440	67.8674±0.1824	93.4917±0.0202	68.5025±0.1026	74.8105±0.1361	71.4768±0.3003
Swin Transformer	93.2645±0.0213	85.9297±0.0436	64.8995±0.2008	93.6117±0.0207	69.4373±0.1047	67.9535±0.1534	69.7311±0.3287
RealMNet(Ours)	97.1399±0.0139	97.1671±0.0139	98.3832±0.0145	96.3504±0.0170	95.8280±0.0194	97.5641±0.0199	99.1062±0.0160
RealMNet-Max(Ours)	97.1369±0.0140	97.1838±0.0140	98.5153±0.0140	96.4073±0.0170	95.9304±0.0186	98.0075±0.0164	98.9830±0.0248

Table 4: Model information.

Model	Architecture	Implementation	Scale	Image Size	#Params(M)	FLOPs(G)
DeiT	Transformer	Distillation	Base	384	87.63	55.65
ConvNeXt	ConvNet	Hierarchy	Tiny	384	28.59	13.14
EfficientNet	ConvNet	Scaling	B4	380	19.34	4.66
Swin Transformer	Transformer	Hierarchy	Base	384	87.90	44.49
RealMNet (Ours)	Hybrid	Hierarchy Pretraining	21M	384	21.23	13.85
RealMNet (Ours)	Hybrid	Hierarchy Pretraining	21M	512	21.27	27.15

Table 5: Data overview of the centralized inference protocol (CIP).

Protocol	Training set		Development set		Testing set	
	Patients	Images	Patients	Images	Patients	Images
CIP	3,192 (r. 3,138)	30,420 (r. 24,683)	684	6,377	684	6,574

The numbers with prefix r. mean resampling results.

Table 6: Data overview of the main-source robustness protocol (MRP).

Protocol	Training set			Testing set		
	Subset	Patients	Images	Subset	Patients	Images
MRP	ShenzhenEye	4,003 (r. 3,944)	38,922 (r. 31,575)	SUSTech	226	2,835
				LishuiR	155	938
				Zhongshan	85	456
				LishuiZ	91	220

The numbers with prefix r. mean resampling results.

Table 7: Data overview of the cyclic-source generalizability protocol (CGP).

Protocol	Training set			Testing set		
	Subset	Patients	Images	Subset	Patients	Images
CGP	PSMM (w/o SUSTech)	4,334 (r. 4,256)	40,536 (r. 32,888)	SUSTech	226	2,835
	PSMM (w/o LishuiR)	4,405 (r. 4,330)	42,433 (r. 34,408)	LishuiR	155	938
	PSMM (w/o Zhongshan)	4,475 (r. 4,398)	42,915 (r. 34,871)	Zhongshan	85	456
	PSMM (w/o LishuiZ)	4,469 (r. 4,389)	43,151 (r. 35,009)	LishuiZ	91	220

The numbers with prefix r. mean resampling results.

696 **Appendix A Extended Data**

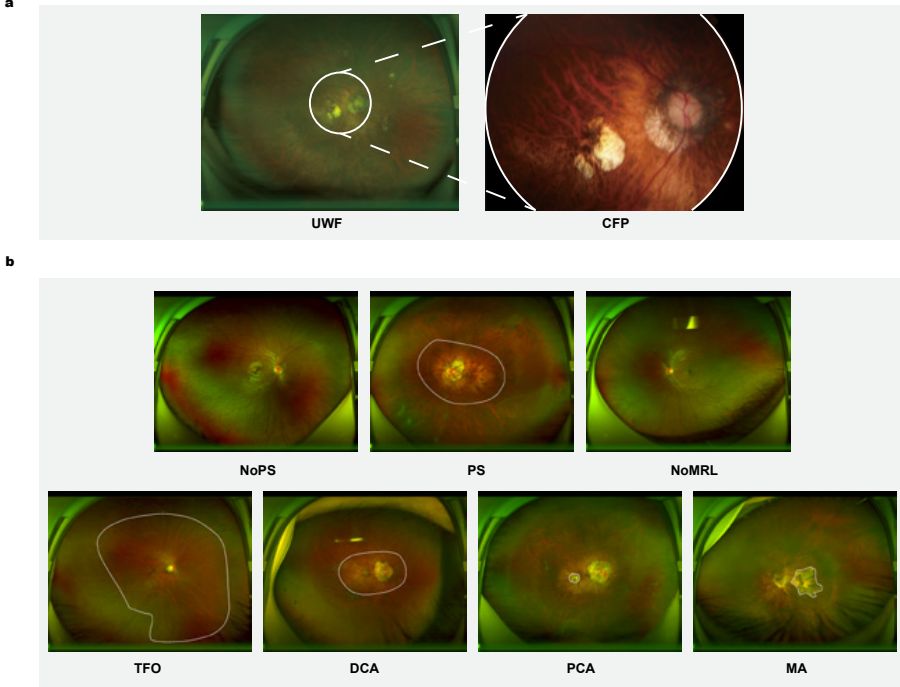


Fig. A1: Illustration of ultra-widefield imaging and lesion types on the PSMM dataset. **a**, Retinal field of view comparison between ultra-widefield (UWF) imaging and color fundus photography (CFP). We present UWF and CFP images from the same patient to illustrate the expanded field of view provided by UWF imaging. **b**, Lesion regions of posterior staphyloma and myopic maculopathy. We show the presence of posterior staphyloma (NoPS or PS) and five categories of myopic maculopathy: no myopic retinal lesions (NoMRL), tessellated fundus only (TFO), diffuse chorioretinal atrophy (DCA), patchy chorioretinal atrophy (PCA), and macular atrophy (MA).

697 We introduce the seven categories of posterior staphyloma and myopic maculopathy
 698 annotated in the PSMM dataset, along with their corresponding lesion regions of
 699 clinical interest. Different types of lesions require different areas of concern, making
 700 accurate segmentation challenging and posing a subsequent challenge for further work.

701 It can be observed that the data collected are mainly concentrated on young adults
 702 requiring timely diagnosis and treatment. Data on younger and older patients have
 703 also been collected to provide a more comprehensive perception. While some datasets
 704 often collect data that are balanced in terms of age and gender, we prioritize gathering
 705 real-world data to support the development of models that can handle imbalanced

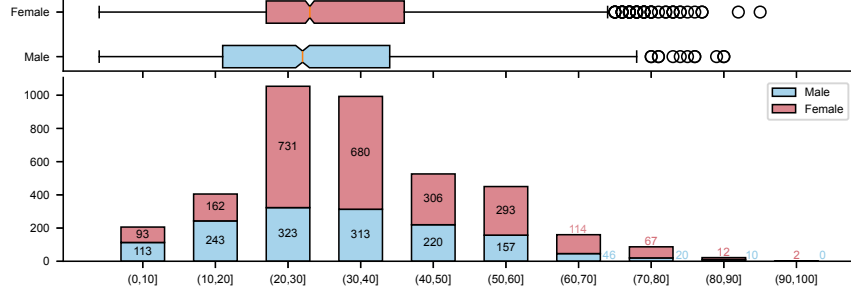


Fig. A2: Statistics of age and gender of the ShenzhenEye subset. The histogram presents the number of males and females within each ten-year age interval, while the box plot illustrates the distribution of ages.

706 data. Although this approach may lead to lower model performance, it is essential to
707 have the courage to confront these challenges.

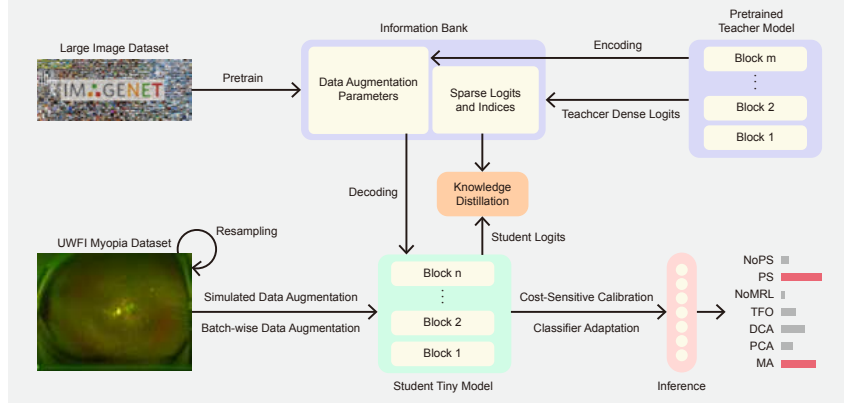


Fig. A3: Architecture details of RealMNet. RealMNet harnesses the TinyViT as the feature extraction backbone. The process of pretraining distillation is explained, and the resulting distilled student model is employed for fine-tuning to tackle the challenge of identifying posterior staphyloma and myopic maculopathy.

708 Resampling methods are essential for addressing the imbalance issue in multi-label
709 datasets (MLDs). Researchers have developed various algorithms to tackle different
710 MLDs and minimize the potential adverse effects of imbalanced data distributions.
711 In this study, we examine six widely adopted approaches (Fig. A5a). LP-ROS (Label
712 Powerset Random Over Sampling) [42] is a method that oversamples multi-label
713 datasets by cloning random samples of minority label sets until the dataset is $r\%$
714 larger than the original. LP-RUS (Label Powerset Random UnderSampling) [42] is a

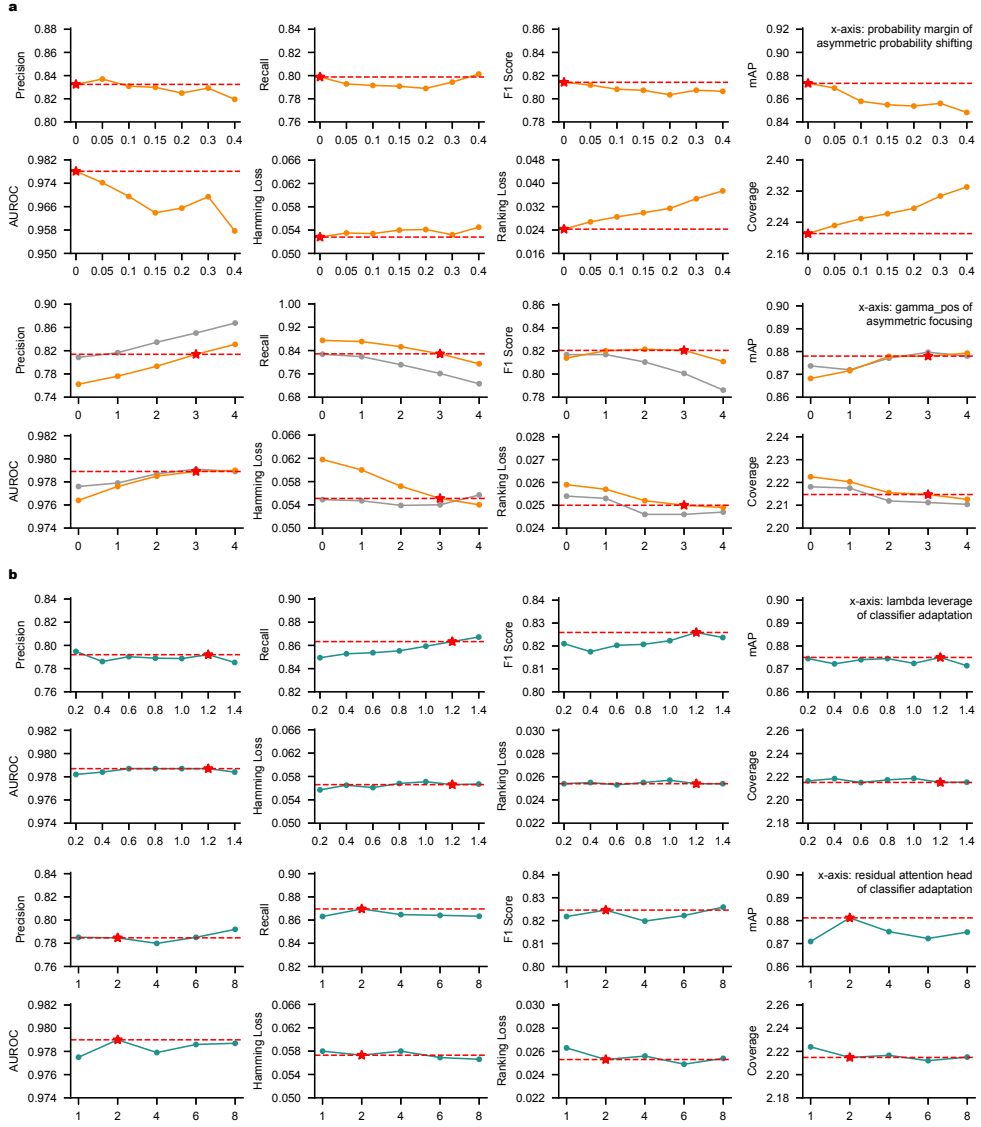


Fig. A4: Researching the advancement of cost-sensitive calibration and classifier adaptation. **a**, We entail an exploration of asymmetric probability shifting and asymmetric focusing, with a search for the probability margin m . In the illustrated results, the gray lines denote the negative focusing parameter $\gamma_- = 2$, while the other colored lines represent $\gamma_- = 4$. **b**, We progressively examine the leveraging parameter λ and the quantity of residual attention head. The determined choice is highlighted with a red star, accompanied by a horizontal line to facilitate comparison.

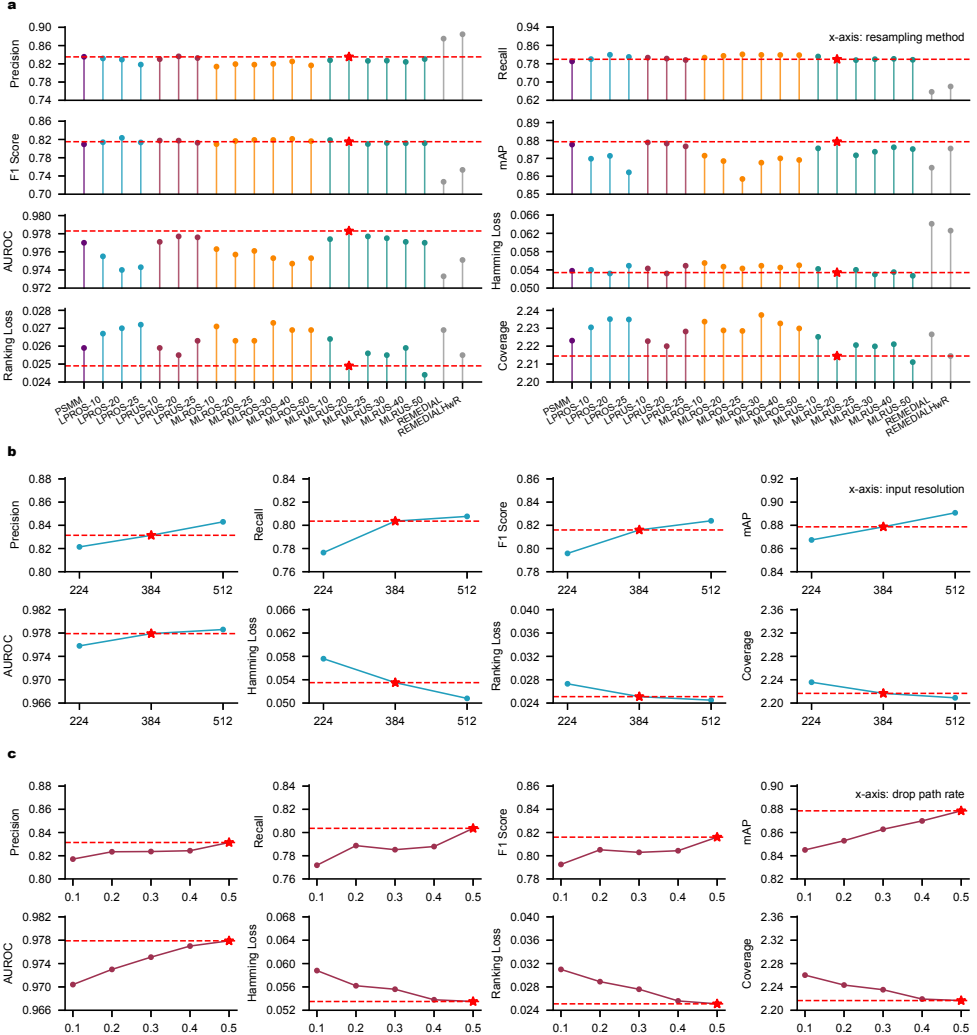


Fig. A5: Comparing model performance using various resampling methods, input resolutions, and drop path rates. **a**, Investigating the resampling methods. We resample the training set using multiple resampling methods: LP-ROS, LP-RUS, ML-ROS, ML-RUS, REMEDIAL, and REMEDIAL-HwR. We explore these methods with various resampling ratios denoted as r . **b**, Investigating the resolutions of input images. We assess common resolutions of 224, 384, and 512 using a development set. **c**, We set a maximum drop path rate of 0.5 with an increment of 0.1 to observe the impact of different drop path rates. The determined choice is highlighted with a red star, accompanied by a horizontal line to facilitate comparison.

715 method that undersamples multi-label datasets by deleting random samples of major-
 716 ity label sets until the dataset is reduced to $(1-r\%)$ of its original size. LP-ROS and
 717 LP-RUS evaluate the frequency of complete label sets during preprocessing. ML-ROS
 718 (Multi-Label Random Over Sampling) [41] identifies samples with minority labels and
 719 clones them, while ML-RUS (Multi-Label Random Under Sampling) [41] identifies
 720 samples with majority labels and deletes them. ML-ROS and ML-RUS evaluate the
 721 frequency of individual labels, isolating samples in which one or more minority labels
 722 appear. REMEDIAL (REsampling MultilabEl datasets by Decoupling highly ImbAl-
 723 anced Labels) [43] is an algorithm that edits and oversamples by decoupling frequent
 724 and rare classes appearing in the same sample and adding new samples to the original
 725 dataset.

726 Let N be the sample number of a multi-label dataset, L the full set of labels, λ the
 727 label being analyzed, and \mathbf{y}_i the label set of i -th sample. We use the IRLbl (Imbalance
 728 Ratio per Label) measure that is calculated individually for each label:

$$\text{IRLbl}(\lambda) = \frac{\max_{\lambda' \in L} \left(\sum_{i=1}^N [\![\lambda' \in \mathbf{y}_i]\!] \right)}{\sum_{i=1}^N [\![\lambda \in \mathbf{y}_i]\!]}$$

729 where the symbol $[\![\cdot]\!]$ denotes the Iverson bracket, which returns 1 if the expression
 730 inside it is true or 0 otherwise. The higher the IRLbl, the larger would be the imbalance,
 731 which helps identify minority or majority labels. Then, we calculate the MeanIR (Mean
 732 Imbalance Ratio) measure by averaging IRLbl to estimate the global imbalance level:

$$\text{MeanIR} = \frac{1}{L} \sum_{\lambda \in L} \text{IRLbl}(\lambda)$$

733 The REMEDIAL algorithm is calculated relying on the SCUMBLE (Score of Con-
 734 currence among iMBalanced LabEls) measure that aims to quantify the imbalance
 735 variance among the labels present in each data sample. SCUMBLE is based on the
 736 Atkinson index and the IRLbl measure. The SCUMBLE value of each sample in a
 737 multi-label dataset D is calculated as follows:

$$\text{SCUMBLE}_{\text{sample}}(s) = 1 - \frac{1}{\overline{\text{IRLbl}_s}} \left(\prod_{\lambda=1}^L \text{IRLbl}_s(\lambda) \right)^{(1/L)}$$

738 where $\text{IRLbl}_s(\lambda) = \text{IRLbl}(\lambda)$ if the label λ is present in the sample s , otherwise 0.
 739 $\overline{\text{IRLbl}_s}$ stands for the average imbalance level of the labels appearing in sample s . We
 740 average all scores of samples to obtain the final SCUMBLE value:

$$\text{SCUMBLE}_{\text{dataset}}(D) = \frac{1}{L} \sum_{\lambda=1}^L \text{SCUMBLE}_{\text{sample}}(\lambda)$$

741 We also harness the SCUMBLELbl to leverage the difficulty of labels:

$$\text{SCUMBLELbl}(\lambda) = \frac{\sum_{i=1}^N [\![\lambda \in \mathbf{y}_i]\!] \cdot \text{SCUMBLE}_{sample}(s)}{\sum_{i=1}^N [\![\lambda \in \mathbf{y}_i]\!]}$$

742 Based on our evaluation, ML-ROS and ML-RUS outperform LP-ROS and LP-RUS
743 in terms of mAP and AUROC, despite having similar F1 Score results. Therefore,
744 we investigate the performance of ML-ROS and ML-RUS with more compact resam-
745 pling ratios. Our findings indicate that ML-RUS surpasses ML-ROS in both mAP
746 and AUROC, while also exhibiting lower Hamming Loss, Ranking Loss, and Cover-
747 age. We also observe that both the REMEDIAL algorithm and its adapted version,
748 REMEDIAL-HwR, do not yield better performance. This confirms that REMEDIAL
749 performs poorly on multi-label datasets with a low SCUMBLE level, which in our case
750 is 0.0741. As a result, we opt for the ML-RUS algorithm with a resampling ratio of
751 $r = 20$, as it consistently excels across all evaluation metrics.

752 The choice of resolution directly impacts the quality of features the model can
753 learn. Most neural networks use resolutions like 224, 256, and 384. We test different
754 resolutions on a development set to see how they affect model performance (Fig. A5b).
755 Our backbone is designed to work with a resolution of 512, which is larger than typi-
756 cal backbones. When we fine-tune the model using higher resolutions, we increase the
757 window size of each self-attention layer to match the input resolution. Our results show
758 that higher resolutions lead to more accurate results, but they require more training
759 time and computational resources. After considering performance and resource require-
760 ments, we choose 384 as our main resolution for model development. Ultimately, we
761 also scale up the resolution to 512 to demonstrate model capability.

762 Drop path [27] is a critical regularization technique that involves randomly drop-
763 ping entire neural paths to prevent model over-fitting. Since the size of the collected
764 dataset is still relatively small compared to those in computer vision, this technique
765 plays a significant role in constraining the model to fit our tasks. Experimental results
766 (Fig. A5c) show that using a higher drop path rate benefits the model by effectively
767 preventing over-fitting. Therefore, we decide to use a drop path rate of 0.5 for the rest
768 of the experiments in this study.

769 Modern ultra-widefield imaging inevitably photos the boundaries of the physical
770 devices along with the imaging targets, which occlude partial information. To assess
771 whether these boundaries negatively affect the model's inference capability, we intend
772 to segment out these boundaries and re-train our model using data without them. We
773 discover that nearly three-quarters of the images in the PSMM dataset have signifi-
774 cant black borders, and the remaining images, while lacking black borders, still show
775 considerable device boundary interference. We randomly sample 1% of the data from
776 the two imaging types to construct a segmentation dataset. We select at the patient
777 level to circumvent the information leakage emphasized in the stratified partitioning.
778 We seek the expertise of professional physicians to annotate the dataset at the pixel
779 level. The resulting segmentation dataset comprises 412 images, involving 303 images
780 with black borders and 109 images without black borders. We divide the dataset into

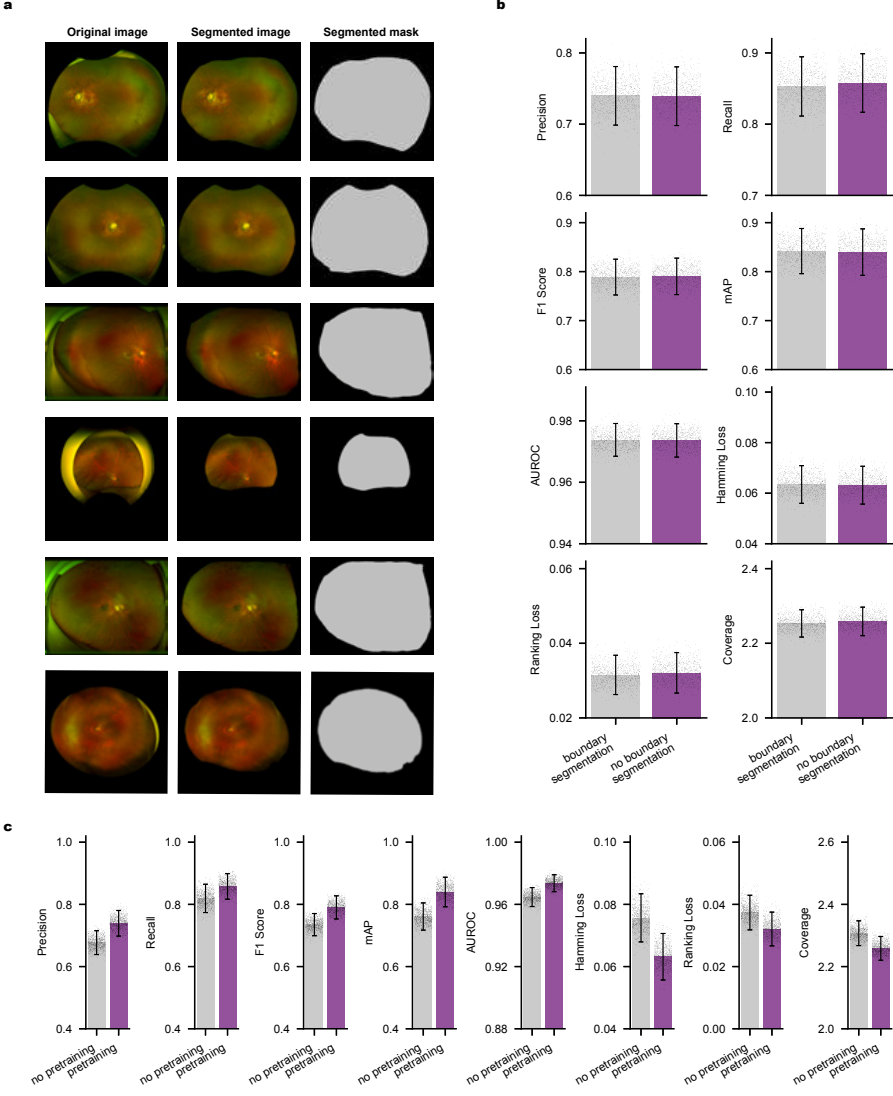


Fig. A6: Investigating the impact of physical device boundaries and pre-training on the model performance. **a**, Visualizing the results of boundary segmentation. We present original images, segmented images, and segmented masks, respectively. **b**, Comparing the performance of models trained on data with and without boundary segmentation. **c**, Comparing the performance of models trained with and without weights derived from large-scale natural image datasets (e.g., ImageNet-21k).

781 a training set, development set, and testing set in an 8:1:1 ratio. We employ ResNet-
782 50 as the segmentation backbone and DeepLab-v3 as the segmentation model with
783 weights trained on the PASCAL Visual Object Classes Challenge (PASCAL VOC)
784 2012 dataset [44]. We utilize the SGD optimizer with a batch size of 4, a learning
785 rate of 0.01, and a momentum of 0.9 for 2,000 epochs with early stopping. After fine-
786 tuning, we harness the model to segment out the boundaries of the physical devices
787 and re-train RealMNet with these images. Ultimately, we find that there is hardly
788 any difference between the performance of models trained on data with and with-
789 out boundary segmentation, which suggests that the model distinguishes instrumental
790 regions and focuses the field of view within the boundaries of the physical devices.

791 We demonstrate the effectiveness of pretraining by observing the advantages gained
792 from distilling the pretraining of the backbone on large-scale natural image datasets,
793 such as ImageNet-21k [45]. Training a model from scratch requires a large dataset
794 and a significant amount of time. Pretraining allows for the transfer of knowledge to
795 downstream tasks, improving performance and reducing the need to start training from
796 scratch. It can also conserve computational resources by utilizing the already learned
797 representations. We find that the performance of the model improves significantly
798 when initialized with weights that encompass the abundant knowledge from the large-
799 parametric model (in our case, CLIP-ViT-L/14-21k [46]), which demonstrates the
800 superiority of utilizing the power of pertaining.

Table A1: Overview of the PSMM dataset and its subsets.

Dataset	Source	Patients	UWF Images
PSMM	Integrated	4,560	43,371
ShenzhenEye	Main	4,003	38,922
SUSTech	Auxiliary	226	2,835
LishuiR	Auxiliary	155	938
Zhongshan	Auxiliary	85	456
LishuiZ	Auxiliary	91	220

Table A2: Imbalance levels of the PSMM dataset.

Measure	NoPS	PS	NoMRL	TFO	DCA	PCA	MA
IRLbl	1.1145	2.0999	15.4234	1.	5.0833	11.5897	38.9930
SCUMBLELlbl	0.0394	0.1393	0.4986	0.0124	0.0915	0.2853	0.5596
w/ REMEDIAL	0.0018	0.0606	0.	0.0124	0.0915	0.	0.
MeanIR				10.7577			
SCUMBLE				0.0741 (w/ REMEDIAL 0.0174)			

Table A3: Black border statistics for image data of the PSMM dataset and its subsets.

Dataset	PSMM	ShenzhenEye	SUSTech	LishuiR	Zhongshan	LishuiZ
w/ Black Border	31,244	28,409	2,835	0	0	0
w/o Black Border	12,127	10,513	0	938	456	220

Table A4: Boundary segmentation results.

Boundary Segmentation	Accuracy	mIoU
w/ Black Border	0.9813	0.9586
w/o Black Border	0.9796	0.9482

Table A5: Varying α for Cross-Entropy Loss ($\gamma = 0$).

α	Precision	Recall	F1 Score	mAP	AUROC	Hamming Loss \downarrow	Ranking Loss \downarrow	Coverage \downarrow
.10	0.9071	0.6071	0.7105	0.8778	0.9766	0.0659	0.0255	2.2233
.25	0.8720	0.7325	0.7922	0.8783	0.9774	0.0554	0.0249	2.2145
.50	0.8309	0.8031	0.8158	0.8794	0.9781	0.0541	0.025	2.2156
.75	0.7805	0.8716	0.8229	0.8787	0.9782	0.0575	0.0253	2.2148
.90	0.7163	0.9347	0.8082	0.8781	0.9783	0.0709	0.0247	2.2108
.99	0.5193	0.9914	0.6569	0.8492	0.9747	0.1389	0.0254	2.2194
.999	0.3981	0.9961	0.5186	0.7532	0.9607	0.2545	0.0314	2.2614

Table A6: Varying γ for Focal Loss (with optimal α).

γ	α	Precision	Recall	F1 Score	mAP	AUROC	Hamming Loss \downarrow	Ranking Loss \downarrow	Coverage \downarrow
0	.75	0.7805	0.8716	0.8229	0.8787	0.9782	0.0575	0.0253	2.2148
0.1	.75	0.7822	0.8693	0.8230	0.8764	0.9787	0.0571	0.0251	2.2134
0.2	.75	0.7826	0.8688	0.8230	0.8779	0.9788	0.0569	0.0248	2.2109
0.5	.50	0.8296	0.7981	0.8122	0.8774	0.9786	0.0537	0.0249	2.2133
1.0	.25	0.8628	0.7207	0.7806	0.8747	0.9774	0.0566	0.0252	2.2156
2.0	.25	0.8660	0.7180	0.7802	0.8768	0.9783	0.0564	0.0251	2.2142
5.0	.25	0.8695	0.7097	0.7760	0.8791	0.9790	0.0572	0.0253	2.2155

Table A7: Varying T_P and T_N for Two-way Loss.

T_P	T_N	Precision	Recall	F1 Score	mAP	AUROC	Hamming Loss \downarrow	Ranking Loss \downarrow	Coverage \downarrow
0.5	0.5	0.7493	0.8883	0.8124	0.8803	0.9774	0.0668	0.0261	2.2241
0.5	1	0.7095	0.922	0.8006	0.8821	0.978	0.0773	0.0254	2.2153
0.5	2	0.6787	0.9453	0.7871	0.8837	0.9788	0.0878	0.0246	2.2075
0.5	4	0.6531	0.9591	0.77	0.8851	0.9785	0.0948	0.0246	2.2075
1	0.5	0.7729	0.8694	0.8178	0.8736	0.9764	0.0607	0.0262	2.2272
1	1	0.7244	0.9072	0.804	0.8771	0.9772	0.0699	0.025	2.2159
1	2	0.6938	0.9388	0.7949	0.8812	0.9783	0.0797	0.0241	2.2073
1	4	0.6548	0.9571	0.7704	0.8802	0.9781	0.0918	0.0245	2.2101
2	0.5	0.798	0.837	0.8162	0.8699	0.9752	0.0568	0.0261	2.2288
2	1	0.7536	0.8835	0.8123	0.8734	0.9769	0.0629	0.025	2.2186
2	2	0.714	0.9226	0.8025	0.8761	0.9777	0.0712	0.0243	2.2103
2	4	0.6691	0.9532	0.7778	0.8771	0.9781	0.0817	0.0238	2.2043
4	0.5	0.8294	0.7918	0.806	0.8675	0.9745	0.0557	0.0263	2.2293
4	1	0.8017	0.8371	0.8164	0.8702	0.9761	0.0578	0.0259	2.2241
4	2	0.7475	0.885	0.809	0.8708	0.9763	0.0639	0.0252	2.2161
4	4	0.6853	0.9424	0.7852	0.8688	0.9759	0.073	0.025	2.2117

801 References

- 802 [1] Baird, P.N., Saw, S.-M., Lanca, C., Guggenheim, J.A., Smith III, E.L., Zhou,
803 X., Matsui, K.-O., Wu, P.-C., Sankaridurg, P., Chia, A., *et al.*: Myopia. *Nature*
804 reviews Disease primers **6**(1), 99 (2020)
- 805 [2] Dolgin, E.: A myopia epidemic is sweeping the globe. here's how to stop it. *Nature*
806 **629**(8014), 989–991 (2024)
- 807 [3] Morgan, I.G., Ohno-Matsui, K., Saw, S.-M.: Myopia. *The Lancet* **379**(9827),
808 1739–1748 (2012)
- 809 [4] Choudhry, N., Golding, J., Manry, M.W., Rao, R.C.: Ultra-widefield steering-
810 based spectral-domain optical coherence tomography imaging of the retinal
811 periphery. *Ophthalmology* **123**(6), 1368–1374 (2016)
- 812 [5] Dai, L., Wu, L., Li, H., Cai, C., Wu, Q., Kong, H., Liu, R., Wang, X., Hou, X.,
813 Liu, Y., *et al.*: A deep learning system for detecting diabetic retinopathy across
814 the disease spectrum. *Nature communications* **12**(1), 3242 (2021)
- 815 [6] Bora, A., Balasubramanian, S., Babenko, B., Virmani, S., Venugopalan, S.,
816 Mitani, A., Oliveira Marinho, G., Cuadros, J., Ruamviboonsuk, P., Corrado, G.S.,
817 *et al.*: Predicting the risk of developing diabetic retinopathy using deep learning.
818 *The Lancet Digital Health* **3**(1), 10–19 (2021)
- 819 [7] Yim, J., Chopra, R., Spitz, T., Winkens, J., Obika, A., Kelly, C., Askham,
820 H., Lukic, M., Huemer, J., Fasler, K., *et al.*: Predicting conversion to wet
821 age-related macular degeneration using deep learning. *Nature Medicine* **26**(6),
822 892–899 (2020)
- 823 [8] Ohno-Matsui, K., Kawasaki, R., Jonas, J.B., Cheung, C.M.G., Saw, S.-M., Ver-
824 hoeven, V.J., Klaver, C.C., Moriyama, M., Shinohara, K., Kawasaki, Y., *et*
825 *al.*: International photographic classification and grading system for myopic
826 maculopathy. *American journal of ophthalmology* **159**(5), 877–883 (2015)
- 827 [9] Ohno-Matsui, K., Lai, T.Y., Lai, C.-C., Cheung, C.M.G.: Updates of pathologic
828 myopia. *Progress in retinal and eye research* **52**, 156–187 (2016)
- 829 [10] De Fauw, J., Ledsam, J.R., Romera-Paredes, B., Nikolov, S., Tomasev, N., Black-
830 well, S., Askham, H., Glorot, X., O'Donoghue, B., Visentin, D., *et al.*: Clinically
831 applicable deep learning for diagnosis and referral in retinal disease. *Nature*
832 *medicine* **24**(9), 1342–1350 (2018)
- 833 [11] Zhou, Y., Chia, M.A., Wagner, S.K., Ayhan, M.S., Williamson, D.J., Struyven,
834 R.R., Liu, T., Xu, M., Lozano, M.G., Woodward-Court, P., *et al.*: A foundation
835 model for generalizable disease detection from retinal images. *Nature* **622**(7981),
836 156–163 (2023)

- 837 [12] Tan, T.-E., Anees, A., Chen, C., Li, S., Xu, X., Li, Z., Xiao, Z., Yang, Y., Lei, X.,
 838 Ang, M., *et al.*: Retinal photograph-based deep learning algorithms for myopia
 839 and a blockchain platform to facilitate artificial intelligence medical research: a
 840 retrospective multicohort study. *The Lancet Digital Health* **3**(5), 317–329 (2021)
- 841 [13] Yang, D., Li, M., Wei, R., Xu, Y., Shang, J., Zhou, X.: Optomap ultrawide field
 842 imaging for detecting peripheral retinal lesions in 1725 high myopic eyes before
 843 implantable collamer lens surgery. *Clinical & Experimental Ophthalmology* **48**(7),
 844 895–902 (2020)
- 845 [14] Lewis, H.: Peripheral retinal degenerations and the risk of retinal detachment.
 846 *American journal of ophthalmology* **136**(1), 155–160 (2003)
- 847 [15] Wu, K., Zhang, J., Peng, H., Liu, M., Xiao, B., Fu, J., Yuan, L.: Tinyvit: Fast
 848 pretraining distillation for small vision transformers. In: *European Conference on
 849 Computer Vision*, pp. 68–85 (2022). Springer
- 850 [16] Touvron, H., Cord, M., Douze, M., Massa, F., Sablayrolles, A., Jégou, H.: Training
 851 data-efficient image transformers & distillation through attention. In: *International Conference on Machine Learning*, pp. 10347–10357 (2021). PMLR
- 853 [17] Tan, M., Le, Q.: Efficientnet: Rethinking model scaling for convolutional
 854 neural networks. In: *International Conference on Machine Learning*, pp. 6105–6114
 855 (2019). PMLR
- 856 [18] Liu, Z., Mao, H., Wu, C.-Y., Feichtenhofer, C., Darrell, T., Xie, S.: A convnet
 857 for the 2020s. In: *Proceedings of the IEEE/CVF Conference on Computer Vision
 858 and Pattern Recognition*, pp. 11976–11986 (2022)
- 859 [19] Liu, Z., Lin, Y., Cao, Y., Hu, H., Wei, Y., Zhang, Z., Lin, S., Guo, B.: Swin trans-
 860 former: Hierarchical vision transformer using shifted windows. In: *Proceedings of
 861 the IEEE/CVF International Conference on Computer Vision*, pp. 10012–10022
 862 (2021)
- 863 [20] Chattopadhyay, A., Sarkar, A., Howlader, P., Balasubramanian, V.N.: Grad-
 864 cam++: Generalized gradient-based visual explanations for deep convolutional
 865 networks. In: *2018 IEEE Winter Conference on Applications of Computer Vision
 866 (WACV)*, pp. 839–847 (2018). IEEE
- 867 [21] De Boer, P.-T., Kroese, D.P., Mannor, S., Rubinstein, R.Y.: A tutorial on the
 868 cross-entropy method. *Annals of operations research* **134**, 19–67 (2005)
- 869 [22] Lin, T.-Y., Goyal, P., Girshick, R., He, K., Dollár, P.: Focal loss for dense object
 870 detection. In: *Proceedings of the IEEE International Conference on Computer
 871 Vision*, pp. 2980–2988 (2017)

- 872 [23] Ridnik, T., Ben-Baruch, E., Zamir, N., Noy, A., Friedman, I., Protter, M., Zelnik-
873 Manor, L.: Asymmetric loss for multi-label classification. In: Proceedings of the
874 IEEE/CVF International Conference on Computer Vision, pp. 82–91 (2021)
- 875 [24] Kobayashi, T.: Two-way multi-label loss. In: Proceedings of the IEEE/CVF
876 Conference on Computer Vision and Pattern Recognition, pp. 7476–7485 (2023)
- 877 [25] Zhu, K., Wu, J.: Residual attention: A simple but effective method for multi-
878 label recognition. In: Proceedings of the IEEE/CVF International Conference on
879 Computer Vision, pp. 184–193 (2021)
- 880 [26] Marcondes, D., Simonis, A., Barrera, J.: Back to basics to open the black box.
881 Nature Machine Intelligence, 1–4 (2024)
- 882 [27] Larsson, G., Maire, M., Shakhnarovich, G.: Fractalnet: Ultra-deep neural net-
883 works without residuals. In: International Conference on Learning Representa-
884 tions (2022)
- 885 [28] Dai, S., Chen, L., Lei, T., Zhou, C., Wen, Y.: Automatic detection of patho-
886 logical myopia and high myopia on fundus images. In: 2020 IEEE International
887 Conference on Multimedia and Expo (ICME), pp. 1–6 (2020). IEEE
- 888 [29] Babenko, B., Mitani, A., Traynis, I., Kitade, N., Singh, P., Maa, A.Y., Cuadros,
889 J., Corrado, G.S., Peng, L., Webster, D.R., *et al.*: Detection of signs of disease in
890 external photographs of the eyes via deep learning. Nature biomedical engineering
891 **6**(12), 1370–1383 (2022)
- 892 [30] Ruiz-Medrano, J., Montero, J.A., Flores-Moreno, I., Arias, L., García-Layana, A.,
893 Ruiz-Moreno, J.M.: Myopic maculopathy: current status and proposal for a new
894 classification and grading system (atn). Progress in retinal and eye research **69**,
895 80–115 (2019)
- 896 [31] Everingham, M., Van Gool, L., Williams, C.K., Winn, J., Zisserman, A.: The
897 pascal visual object classes (voc) challenge. International journal of computer
898 vision **88**, 303–338 (2010)
- 899 [32] Engelmann, J., McTrusty, A.D., MacCormick, I.J., Pead, E., Storkey, A., Bern-
900 abeu, M.O.: Detecting multiple retinal diseases in ultra-widefield fundus imaging
901 and data-driven identification of informative regions with deep learning. Nature
902 Machine Intelligence **4**(12), 1143–1154 (2022)
- 903 [33] Graham, B., El-Nouby, A., Touvron, H., Stock, P., Joulin, A., Jégou, H., Douze,
904 M.: Levit: a vision transformer in convnet’s clothing for faster inference. In: Pro-
905 ceedings of the IEEE/CVF International Conference on Computer Vision, pp.
906 12259–12269 (2021)
- 907 [34] Sandler, M., Howard, A., Zhu, M., Zhmoginov, A., Chen, L.-C.: Mobilenetv2:

- 908 Inverted residuals and linear bottlenecks. In: Proceedings of the IEEE Conference
 909 on Computer Vision and Pattern Recognition, pp. 4510–4520 (2018)
- 910 [35] Roberts, M., Hazan, A., Dittmer, S., Rudd, J.H., Schönlieb, C.-B.: The curious
 911 case of the test set auroc. *Nature Machine Intelligence* **6**(4), 373–376 (2024)
- 912 [36] Wu, X.-Z., Zhou, Z.-H.: A unified view of multi-label performance measures. In:
 913 International Conference on Machine Learning, pp. 3780–3788 (2017). PMLR
- 914 [37] Tsoumakas, G., Katakis, I., Vlahavas, I.: Mining multi-label data. *Data mining*
 915 and knowledge discovery handbook, 667–685 (2010)
- 916 [38] Loshchilov, I., Hutter, F.: Decoupled weight decay regularization. In: Interna-
 917 tional Conference on Learning Representations (2019)
- 918 [39] Zhang, H., Cisse, M., Dauphin, Y.N., Lopez-Paz, D.: mixup: Beyond empirical risk
 919 minimization. In: International Conference on Learning Representations (2018)
- 920 [40] Yun, S., Han, D., Oh, S.J., Chun, S., Choe, J., Yoo, Y.: Cutmix: Regularization
 921 strategy to train strong classifiers with localizable features. In: Proceedings of the
 922 IEEE/CVF International Conference on Computer Vision, pp. 6023–6032 (2019)
- 923 [41] Charte, F., Rivera, A.J., Jesus, M.J., Herrera, F.: Addressing imbalance in multil-
 924 abel classification: Measures and random resampling algorithms. *Neurocomputing*
 925 **163**, 3–16 (2015)
- 926 [42] Charte, F., Rivera, A., Jesus, M.J., Herrera, F.: A first approach to deal with
 927 imbalance in multi-label datasets. In: Hybrid Artificial Intelligent Systems: 8th
 928 International Conference, HAIS 2013, Salamanca, Spain, September 11-13, 2013.
 929 Proceedings 8, pp. 150–160 (2013). Springer
- 930 [43] Charte, F., Rivera, A.J., Jesus, M.J., Herrera, F.: Dealing with difficult minority
 931 labels in imbalanced multilabel data sets. *Neurocomputing* **326**, 39–53 (2019)
- 932 [44] Everingham, M., Van Gool, L., Williams, C.K.I., Winn, J., Zisserman, A.: The PASCAL Visual Object Classes
 933 Challenge 2012 (VOC2012) Results. [http://www.pascal-](http://www.pascal-network.org/challenges/VOC/voc2012/workshop/index.html)
 934 [network.org/challenges/VOC/voc2012/workshop/index.html](http://www.pascal-network.org/challenges/VOC/voc2012/workshop/index.html)
- 935
- 936 [45] Ridnik, T., Ben-Baruch, E., Noy, A., Zelnik-Manor, L.: Imagenet-21k pretrain-
 937 ing for the masses. In: Thirty-fifth Conference on Neural Information Processing
 938 Systems Datasets and Benchmarks Track (Round 1) (2021)
- 939 [46] Radford, A., Kim, J.W., Hallacy, C., Ramesh, A., Goh, G., Agarwal, S., Sastry, G.,
 940 Askell, A., Mishkin, P., Clark, J., *et al.*: Learning transferable visual models from
 941 natural language supervision. In: International Conference on Machine Learning,
 942 pp. 8748–8763 (2021). PMLR